nature photonics

Supplementary information

https://doi.org/10.1038/s41566-024-01455-6

# Multicolour stretchable perovskite electroluminescent devices for user-interactive displays

In the format provided by the authors and unedited

# Table of Contents

## Supplementary Notes

### Supplementary Note 1. Energy transfer between ZnS and PeNPs.

The total intra-particle energy transfer in the PeZS phosphors is largely enabled by photon reabsorption because of the large particle size on the micrometer scale. Meanwhile, the core-shell structure promised a close proximity between ZnS and PeNPs, which also permits nonradiative transfer. As we know, nonradiative energy transfer can occur through exchange (Dexter energy transfer, DET) or (Förster resonance energy transfer, FRET) interactions. DET is a short-range interaction based on the wavefunction overlap of the electronic states between donor and acceptor, usually occurring within 1 nm[1, 2]. In contrast, FRET, a long-range interaction, has been documented to occur at distances extending up to 10 nm[3] (Supplementary Fig. 8a).

In our work, the lengths of the ligands OA (2.2 nm) and APTES (0.8 nm) on PeNPs eliminate the possibility of DET. Additionally, the lowest unoccupied molecular orbital (LUMO) levels of the ligands are positioned above the conduction band (CB) levels of ZnS and PeNPs. These ligands thus represent a high potential barrier that electrons have to tunnel through in the DET process, further precluding the possibility of DET (Supplementary Fig. 8b). However, the gaps between PeNPs and ZnS can remain below 10 nm, thereby facilitating FRET.

Furthermore, the distinct dependencies on donor-acceptor separation can be utilized to distinguish between FRET and DET[4]. The PeNPs were initially coated with several nanometres of $SiO_2$ and subsequently bridged to the ZnS phosphors (resulting in ZnS-PeNPs@$SiO_2$) as a control experiment (Supplementary Fig. 8c). The increased distance between ZnS and PeNPs precludes the occurrence of DET. As depicted in Supplementary Fig. 8d, the ZnS-PeNPs@$SiO_2$ structure also exhibits a shorter donor lifetime compared to the case of ZnS, which can be ascribed to FRET.

Consequently, we deduced that the long-range FRET predominantly governs the nonradiative energy transfer between ZnS and PeNPs in the PeZS particles. However, FRET alone is unlikely to convert all energy from the large ZnS core due to the limited interaction distance, resulting in the leakage of blue light. The photon reabsorption by the thick PeNPs shell thus serves as another crucial mechanism that transforms the escaped blue light into the targeted wavelength. Optimal loading of PeNPs can ensure complete colour conversion without significantly reducing brightness (Supplementary Fig. 9).

**Supplementary Note 2. Impact of PeNP shell on EL performance.**

(1) Luminance.

Our comparative analysis has revealed that the luminance of our blue, green, and red PeACEL devices is slightly lower than that of the blue ACEL device using uncoated ZnS phosphors. This difference in luminance can be primarily attributed to minor energy loss during the spectrum conversion process, such as nonradiative relaxation and light attenuation in the PeNP shell. Nevertheless, it is important to note that the brightness and colour conversion efficiency of our devices significantly surpasses that of ACEL devices fabricated using a physical mixture of phosphors (Supplementary Fig. 12) or those fabricated with additional conversion layers (Supplementary Fig. 13). The exceptional luminance of our devices is the result of several key advantages:

a) Enhanced energy transfer efficiency: The core-shell PeZS phosphors we developed, with ZnS as the core and PeNPs as the shell, enable close proximity between the two components. This facilitates FRET, thereby improving the energy transfer efficiency (Supplementary Note 1).

b) Reduced photon loss: The core-shell structure of the phosphor, coupled with the device's simple architecture, shortens the light's travel path within the device, which diminishes reflection, scattering and absorption by other device components, consequently minimizing photon loss and bolstering light extraction efficiency.

c) Unaltered electric field strength. The nanoscale PeNPs coating avoids noticeable changes in the size of EL phosphors. Consequently, it causes no effect on the thickness of the device's emission layer, preventing substantial brightness loss due to the decreased electrical field strength.

(2) Stability.

ZnS-type phosphors, commonly utilized in ACEL devices, display sensitivity to degradation by atmospheric moisture, oxygen, and other environmental components[5]. This degradation leads to a deterioration of their luminescent properties and a consequent decline in brightness. To mitigate this degradation, surface coating techniques are widely employed, with a variety of materials such as silica, zinc oxide, titanium dioxide, indium oxide, yttrium oxide and indium tin oxide as coatings[6-9].

In the development of our PeZS phosphors, the PeNPs@$SiO_2$ composite coating plays a crucial role as a dense barrier against moisture, as evidenced by the EDS mapping and TEM morphology (Fig. 2b and Supplementary Fig. 5). The efficacy of the coating is also supported by the emission spectra under UV light and an AC electric field, revealing a monochromatic emission peak that signifies a dense coating

(Fig. 1c and Supplementary Fig. 4c).

This dense coating offers enhanced stability to both the PeZS phosphors and PeACEL devices. PeNPs are typically prone to structural degradation when exposed to moisture, which results in significant PL quenching due to their sensitivity to ambient conditions and ionic nature (Supplementary Fig. 15a). In contrast, our PeZS phosphors, even when immersed in water without any extra encapsulation, continue to emit single-peak red luminescence (Supplementary Fig. 15b). This demonstrates that the $SiO_2$ layer effectively protects the PeNPs shell from moisture ingress, thus significantly reducing the risk of moisture penetration to the internal ZnS core. The high long-term storage stability of PeZS phosphors at ambient conditions is also favorable evidence of their high resistance to moisture (Supplementary Fig. 16). The robust stability and durability of PeZS materials contribute to an extended lifespan of PeACEL devices. As shown in Supplementary Fig. 23, after continuous operation for 360 hours at 100 V and 20 kHz, our PeACEL devices retain 68% (blue), 79% (green), and 76% (red) of their initial luminance. In stark contrast, devices employing uncoated ZnS phosphors retain only 29% of their original luminance under the same conditions.

**Supplementary Note 3. Stretchability of stretchable PeACEL device.**

The stretchability of the PeACEL device is intimately associated with the intrinsic properties of the polymer matrix and the electrode material. It is predominantly determined by the constituent showing the lowest stretchability, mirroring a scenario referred to as the barrel effect. This is confirmed by the high stretchability (1000%) demonstrated by the PeACEL device, which employs hydrogels as electrodes (Supplementary Fig. 31). In contrast, the use of silver nanowires (AgNWs) as electrodes facilitates the creation of ultra-thin, easily patternable PeACEL devices.

For the PeACEL devices prepared using AgNWs electrodes, the stretchability depends on the pre-strain level. The resistance changes of pre-strain AgNWs electrodes were measured under various tensile strains (Supplementary Fig 27e,f). The resistances remain relatively low when stretched to 300%, with further stretching resulting in a precipitous increase in resistance. Comparative analysis revealed that the resistance increase in the AgNWs electrode embedded in the device was more pronounced than that of the unencapsulated bottom electrode, which could be attributed to the scraping of the emissive and encapsulation layers. In EL devices, any form of electrode damage can lead to device failure. Hence, when the strain exceeds 400%, EL emission is absent, due to the damage of the bottom electrode.

It should be noted that a higher pre-strain level is conducive to achieving greater stretchability. However, excessively pursuing high pre-strain levels is not advisable as this could result in permanent tensile deformation.

**Supplementary Note 4. Safety evaluation of wearable PeACEL devices.**

**1) Low turn-on and operating voltage.** Contrary to frequency-dependent commercial ACEL devices, our PeACEL devices demonstrate exceptional frequency stability. An increase in frequency allows for a reduction in both the turn-on (25 V) and operating voltages.

**2) Low current.** The degree of danger depends on the magnitude and time of the current flowing through the body. Previous research on the safety of current influencing the body indicates that the administration of 3 mA of current through electrodes does not induce adverse effects, such as skin burns, skin redness or pain[10]. In our PeACEL devices, the maximum current magnitudes injected through the device were only 0.048 and 0.093 mA at operating voltages of 100 and 200 V, respectively, significantly lower than 3 mA.

**3) Insulation layer.** In our wearable PeACEL devices, the electrodes were sealed in the polymer matrix. The dielectric breakdown of the SEBS occurred at around 40 V/μm[11], and the PDMS dielectric breakdown fields varied from 250 to 635 V/μm[12]. With PeACEL devices operating at 100 V, the electric field is about 3 V/μm, significantly lower than the dielectric breakdown voltage. Therefore, there is no risk of breakdown during PeACEL device operation.

**4) Current overload protection.** For the skin display, a driver unit is used instead of a high-voltage power supply, with the output voltage varying from 0 to 100 V and $f_{ac}$ adjusted from 10 to 20 kHz, which is sufficient to drive the PeACEL devices (Fig. 5b and Supplementary Fig. 32). It is powered by a 3.7 V lithium-ion battery and comprises a high-voltage module, current control module, microcontroller unit (MCU), and multiplexer. When a current exceeding a certain limit (e.g., 1 mA) due to leakage is detected, the MCU automatically cuts off the power supply to the high-voltage module.

**5) Biocompatibility.** The mouse embryo fibroblast cell line, NIH/3T3 (ATCC, US), was employed as the model to evaluate *in vitro* cytotoxicity of the PeACEL devices. As revealed by the results of the live/dead staining, the expression of live cells in the SEBS and PeACEL devices was similar to that in the controls, and dead cells were rarely observed, confirming the high biocompatibility of PeACEL devices (Supplementary Fig. 33).

In summary, the low turn-on and operating voltage, small current passage, absence of dielectric breakdown risk, inclusion of an overload protector in the driver unit and non-toxicity collectively affirm the absolute safety of PeACEL devices for wearable and on-skin displays.

## Supplementary Figures

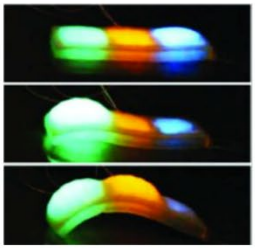

Science 2016, 351, 1071–1074

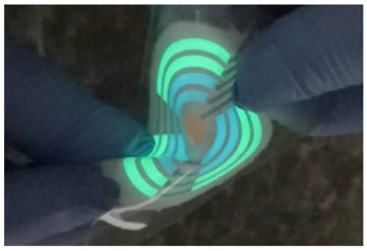

ACS Appl. Mater. Interfaces 2020, 12, 47902-47910

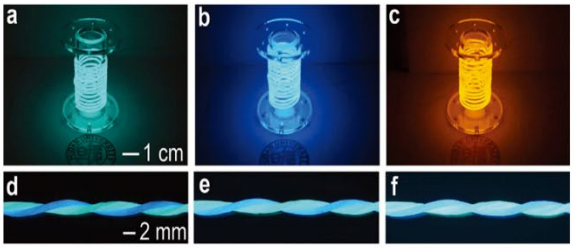


Adv. Mater. 2018, 30, 1800323

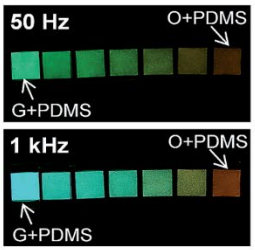


Energy Environ. Sci. 2014, 7, 3338-3346.

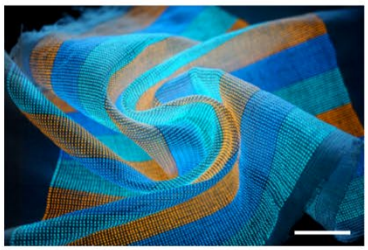

Nature 2021, 591, 240-245.

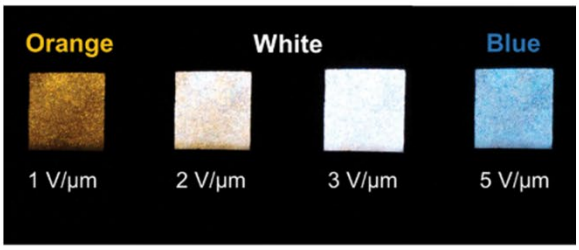


Adv. Funct. Mater. 2020, 30, 2005200

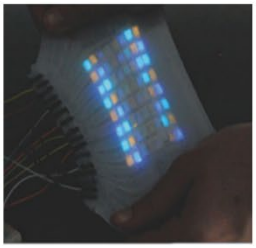

Adv. Mater. 2016, 28, 9770–9775

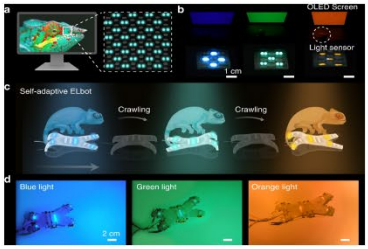


Nat. Commun. 2022, 13, 4775

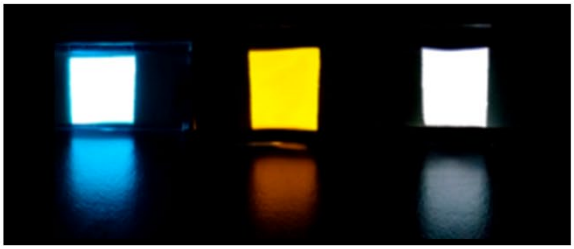

ACS Nano 2020, 14, 3876−3884

**Supplementary Fig. 1 Limited colours in previously reported ACEL devices[13-21].**

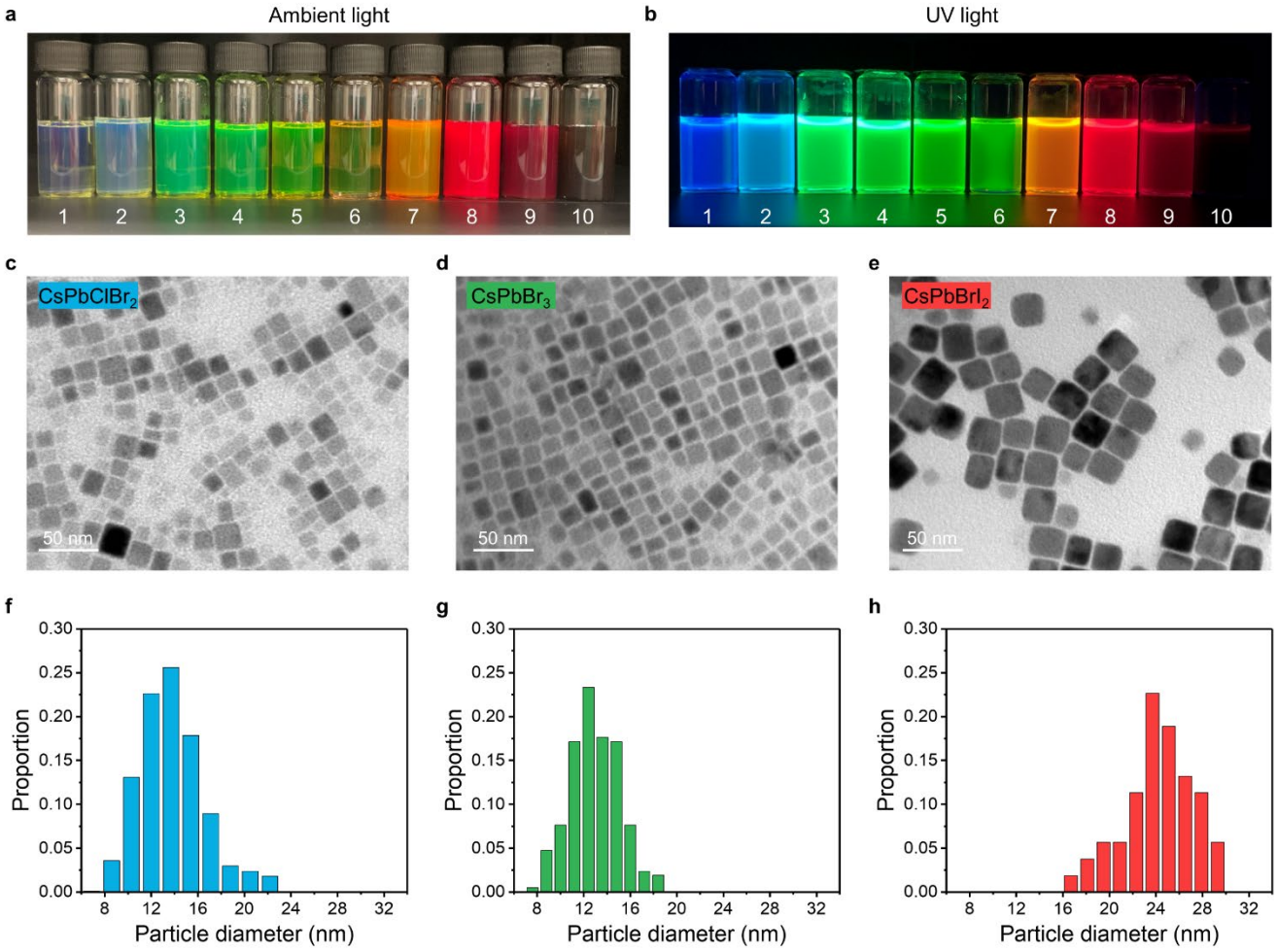


**Supplementary Fig. 2 Characterization of the colour-tunable PeNPs.** (a) Optical image of the PeNPs under ambient light. (b) Optical image of the PeNPs under UV light. (c) TEM image of $CsPbClBr_2$ nanoparticles. (d) TEM image of $CsPbBr_3$ nanoparticles. (e) TEM image of $CsPbBrI_2$ nanoparticles. (f-h) The corresponding size distribution histograms.

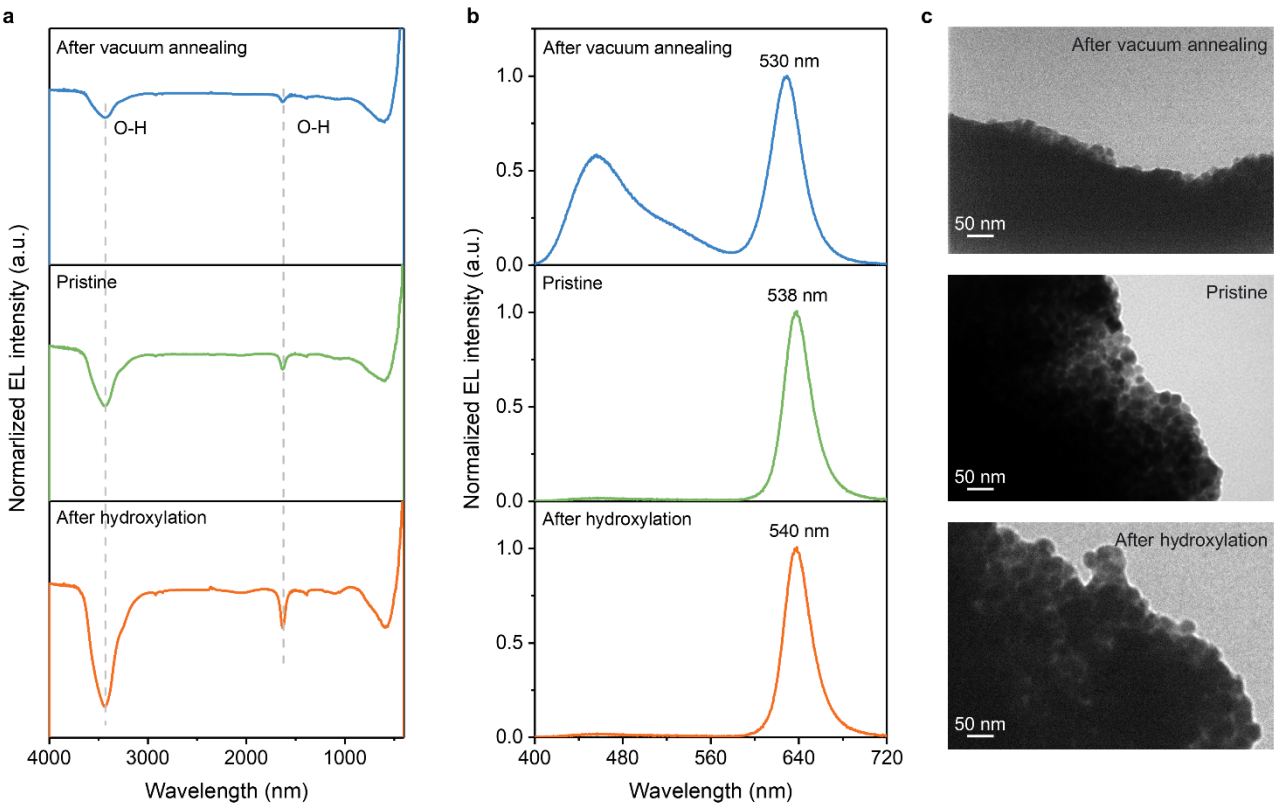


**Supplementary Fig. 3 PeZS phosphors prepared using vacuum-annealed, pristine, and surface hydroxylated ZnS.** (a) FTIR spectra of ZnS. (b) EL spectra of PeZS. (c) TEM images of PeZS. Hydroxyl groups are crucial to the EL performance of PeZS phosphors. The hydroxyl groups on the surface of pristine ZnS phosphors can be attributed to the synthesis process and interactions with water molecules when the phosphors are exposed to the ambient environment. Vacuum annealing and photohydroxylation methods are used to regulate the surface hydroxyl groups of ZnS phosphors. Insufficient hydroxyl group concentration may lead to inadequate surface coverage, thereby compromising colour purity of the emitted light. On the other hand, an increased concentration of hydroxyl groups promotes the formation of thicker coatings under the same reaction conditions, which in turn enhances the reaction process.

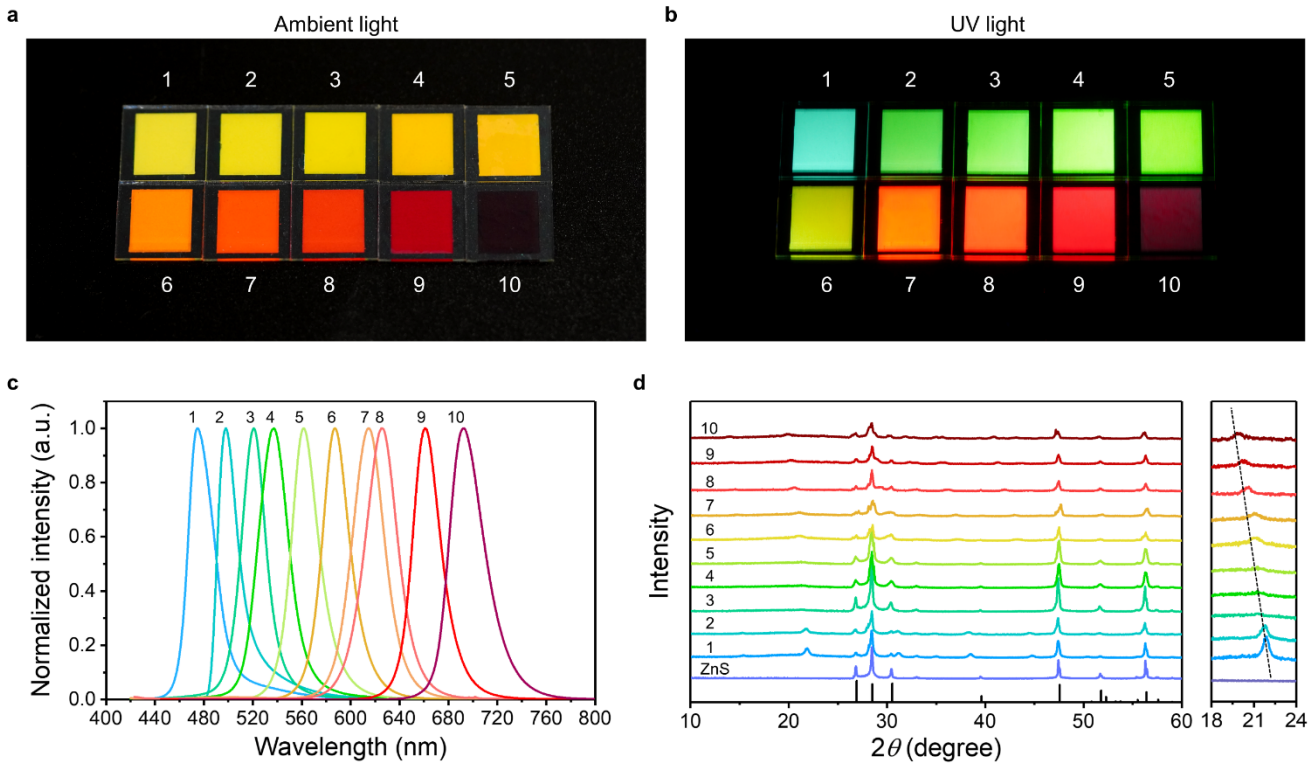


**Supplementary Fig. 4 Characterization of the colour-tunable PeZS phosphors.** (a) Optical image of PeZS/polymer composites under ambient light. (b) Optical image of PeZS/polymer composites under UV light. (c) PL spectra of PeZS phosphors. (d) XRD patterns of PeZS phosphors.

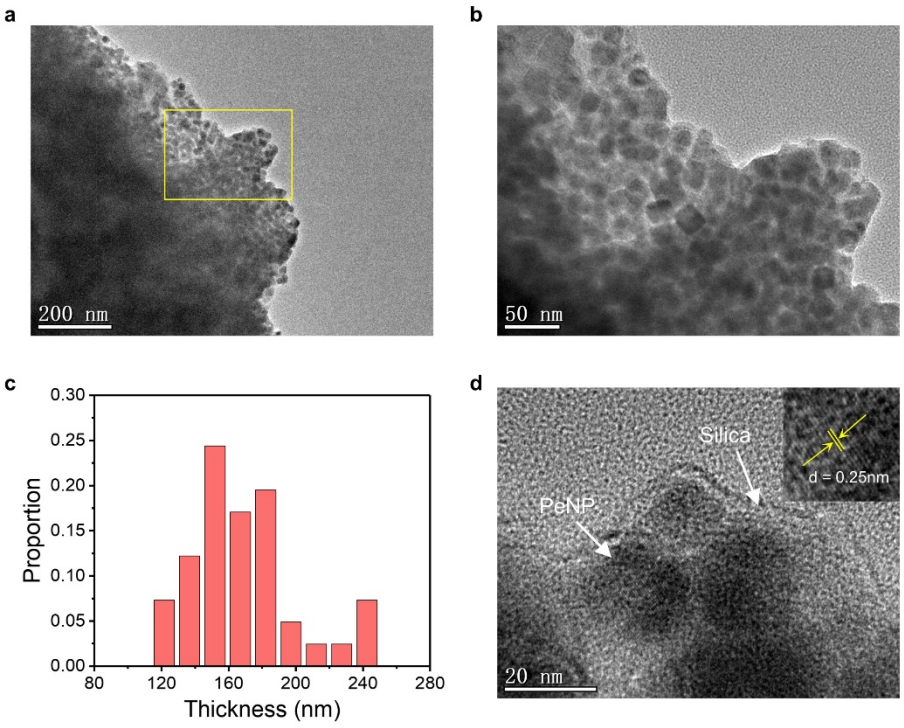


**Supplementary Fig. 5 Microstructure of red-emitting PeZS phosphors.** (a, b) TEM images. (c) Size distribution of the PeNPs coating thickness. (d) High-resolution TEM image.

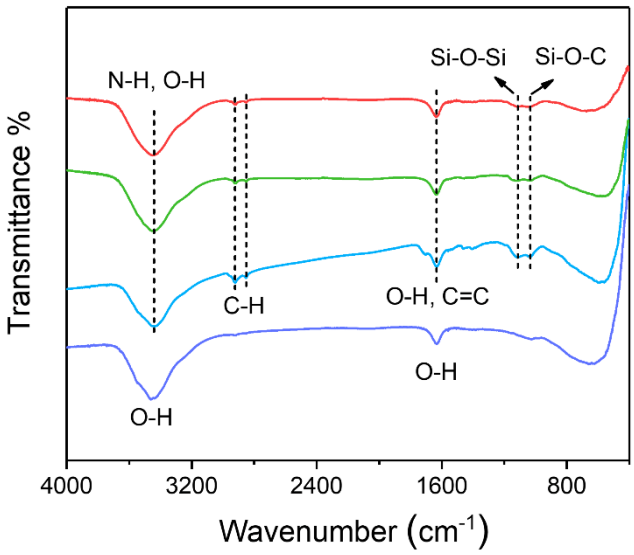


**Supplementary Fig. 6 FTIR spectra of commercial blue ZnS phosphors (purple), blue-emitting PeZS phosphors (blue), green-emitting PeZS phosphors (green), and red-emitting PeZS phosphors (red).**

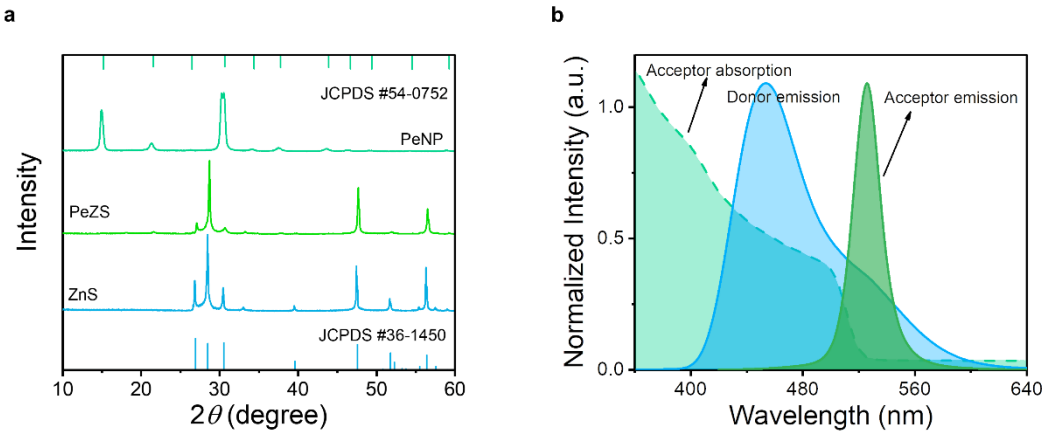


**Supplementary Fig. 7 Characterization of the green PeZS phosphors.** (a) XRD patterns of green PeNPs, commercial ZnS, and green PeZS phosphors. (b) Absorption and emission spectra of green PeNPs and commercial ZnS phosphors.

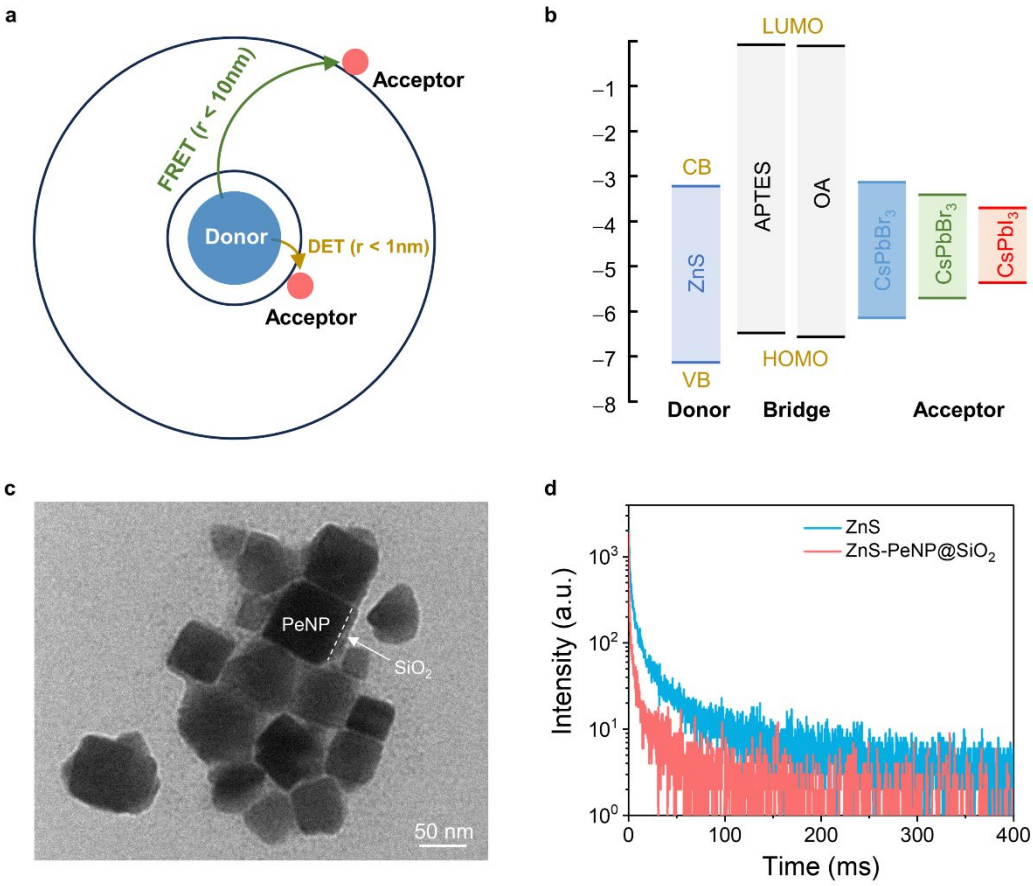


**Supplementary Fig. 8 Intra-particle energy transfer.** (a) Schematic diagram depicting the long-range Förster resonance energy transfer (FRET) and short-range Dexter energy transfer (DET). (b) Conduction and valence band energy levels of ZnS and PeNPs, along with the HOMO-LUMO levels of OA and APTES. (c) TEM images of as-prepared $CsPbBrI_2$@$SiO_2$. (d) Comparison of decay curves of ZnS and ZnS-$CsPbBrI_2$@$SiO_2$ ($\lambda_{exc.}$=370 nm, $\lambda_{collected}$=500 nm).

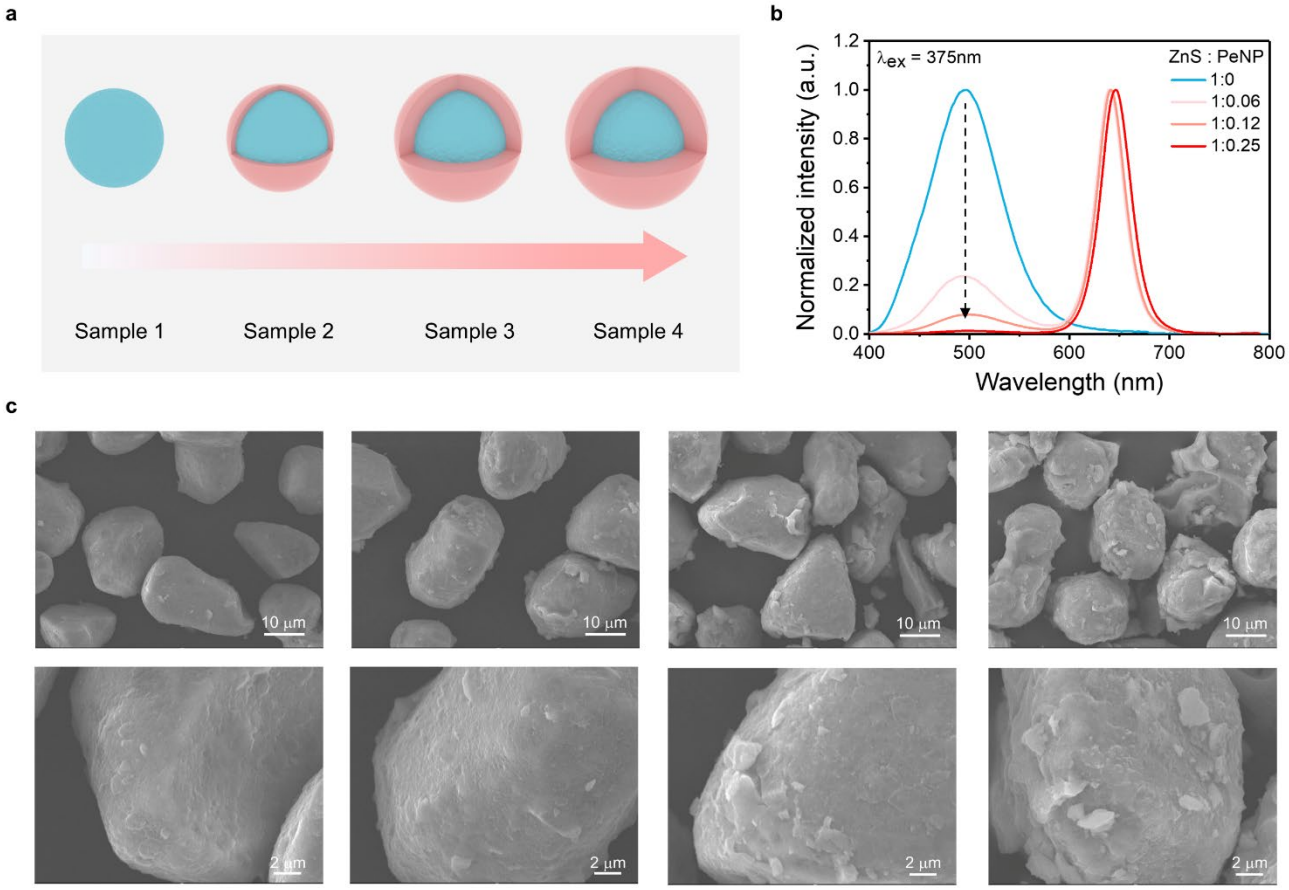


**Supplementary Fig. 9 Characterization of the PeZS phosphors prepared with various amounts of PeNPs.** (a) Schematic illustration of the morphological evolution of PeZS phosphors with increasing PeNPs concentrations. (b) Corresponding PL spectra ($\lambda_{exc.}$=370 nm). (c) Corresponding SEM images and magnified views.

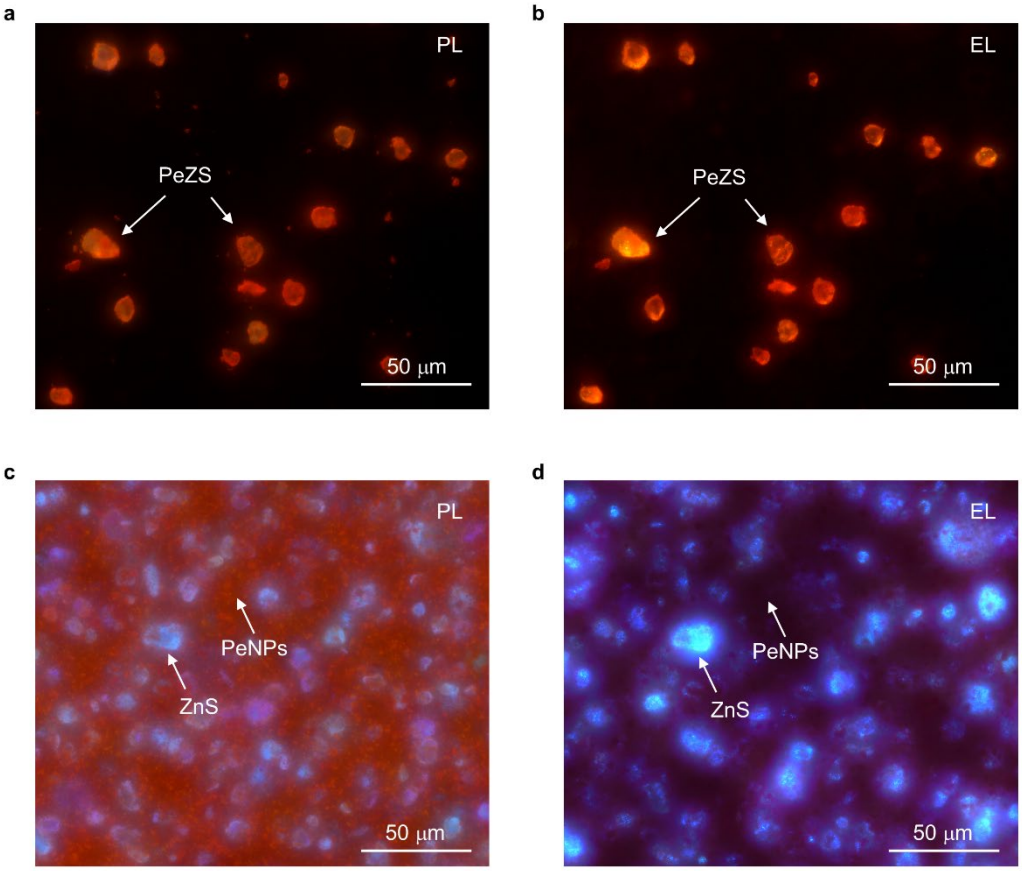


**Supplementary Fig. 10 Comparison of EML under UV light and AC electric field excitation.** (a) Optical micrograph of the PeZS/PDMS EML excited by UV light. (b) Optical micrograph of the PeZS/PDMS EML excited under an AC electric field. (c) Optical micrograph of the mixture EML (ZnS+PeNPs/PDMS) excited by UV light. (d) Optical micrograph of the mixture EML (ZnS+PeNPs/PDMS) excited under an AC electric field.

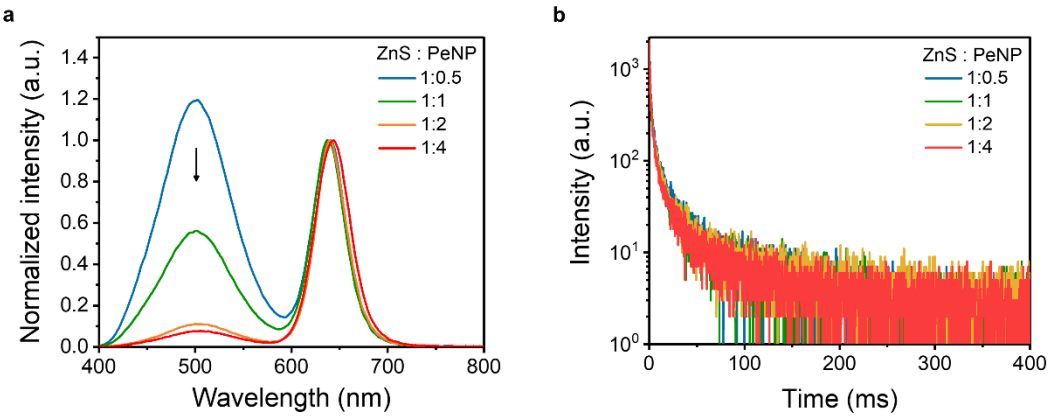


**Supplementary Fig. 11 PL properties of the physically mixed ZnS and PeNPs.** (a) Normalized PL spectra ($\lambda_{exc.}$=370 nm). (b) Lifetime decay curves ($\lambda_{exc.}$=370 nm, $\lambda_{em.}$=500 nm).

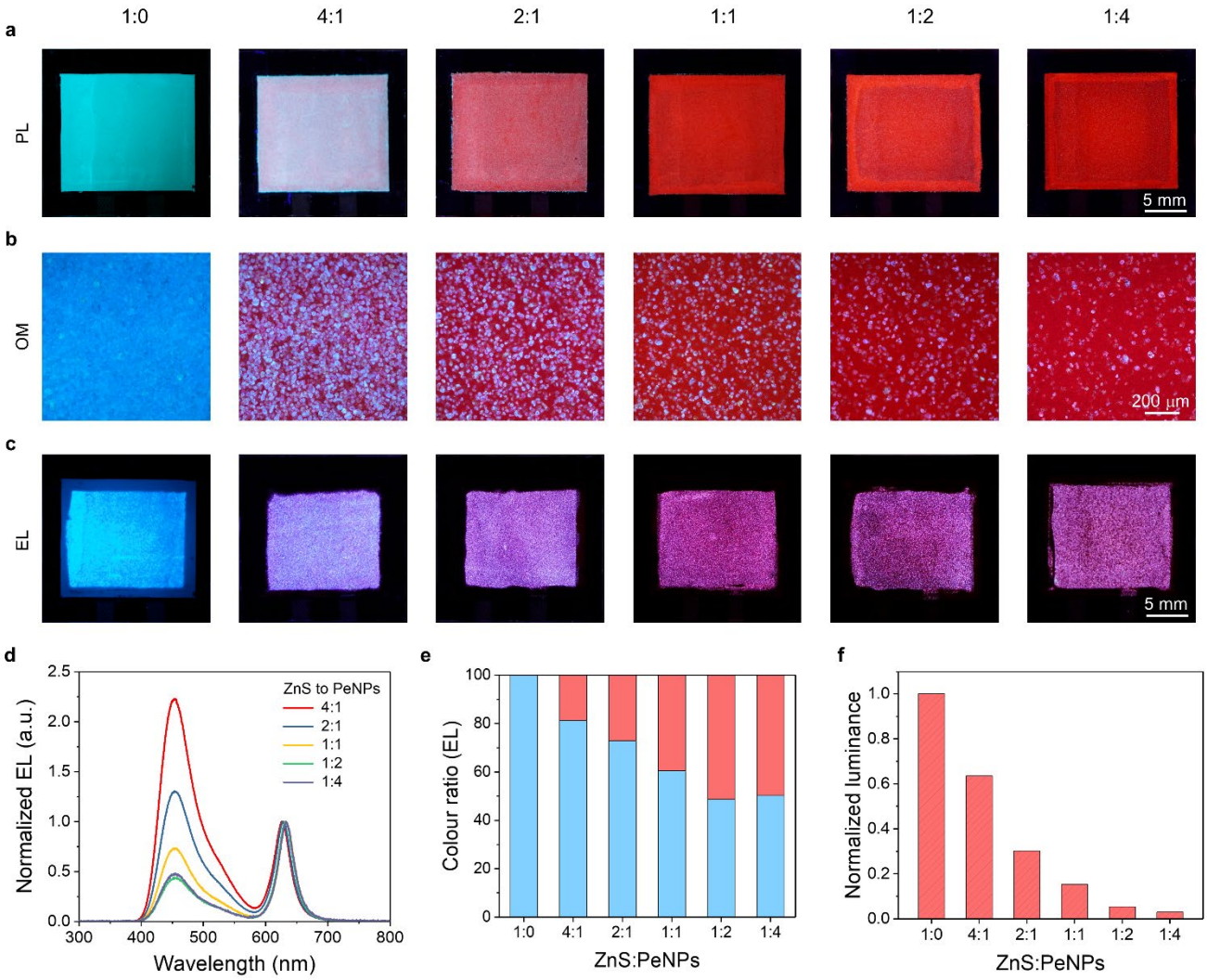


**Supplementary Fig. 12 Characterization of ACEL devices using physically mixed ZnS and red PeNPs at the mass ratios of 1:0, 4:1, 2:1, 1:1, 1:2 and 1:4, respectively.** (a) Photographs of ACEL devices under UV light. (b) Optical micrograph (OM) of ACEL devices excited by UV light. (c) Macro photographs of ACEL devices operating at 100 V with an $f_{ac}$ of 20 kHz. (d) EL spectra of ACEL devices. (e) Colour ratio of EL spectra. (f) Luminance changes of ACEL devices operating at 100 V with an $f_{ac}$ of 20 kHz. As the ratio of PeNPs to ZnS increased, the emitted colour of the fabricated ACEL devices changed from blue to purple and eventually to pink. However, achieving a pure red emission was not possible, as the leakage of blue light could not be eliminated, even when the PeNPs to ZnS ratio was augmented to 4:1. Additionally, a higher proportion of PeNPs had a negative effect on the device's luminance, which is attributable to the significant reduction of ZnS proportion.

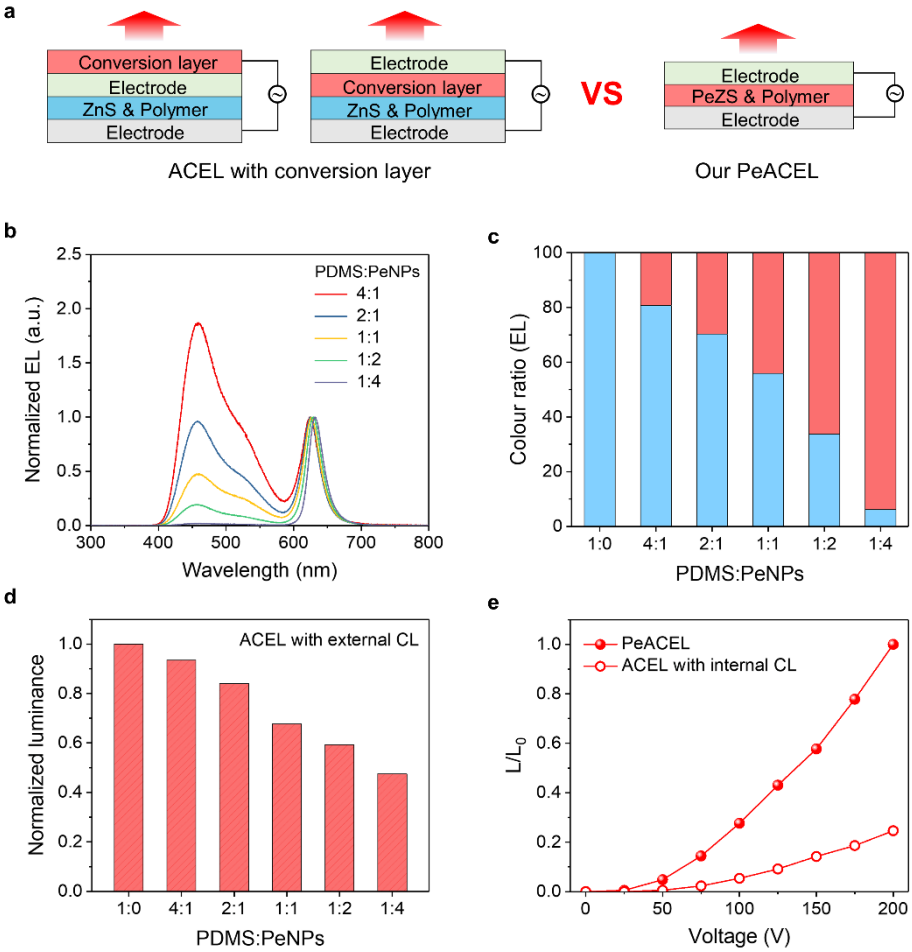


**Supplementary Fig. 13 Comparison of EL performance between ACEL device with conversion layer and our PeACEL device.** (a) Illustrated structures of the red light-emitting devices. ACEL device with external and internal PeNP conversion layer (CL), and PeACEL device using red PeZS phosphors. (b) EL spectra of ACEL devices with a 20 μm conversion layer incorporating different ratios of PDMS to PeNPs. (c) Colour ratios of EL spectra as a function of the varying ratios of PDMS and PeNPs. (d) Effect of external conversion layer on device luminance. (e) A comparison of the luminance of the PeACEL device to that of the ACEL device with an internal conversion layer (20 μm) in terms of operating voltage. The ACEL device's luminance drops to 48% with an external conversion layer and to 25% with an internal layer, due to reflection, scattering, and absorption by other components. The device experiences greater luminance loss with an internal conversion layer, which is attributable to the decreased electric field strength caused by increased electrode spacing.

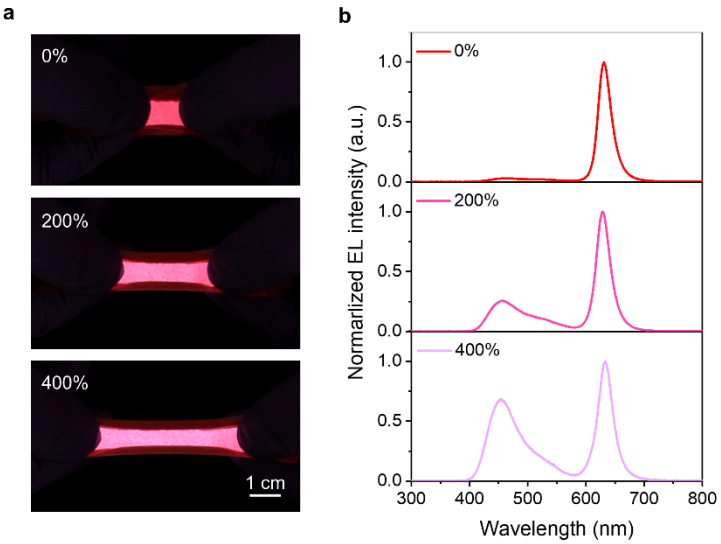


**Supplementary Fig. 14 EL performance of a stretchable ACEL device with a red-emitting conversion layer.** (a) Images and (b) EL spectra of the operating device stretched to different strains. Blue emission becomes increasingly prominent with stretching.

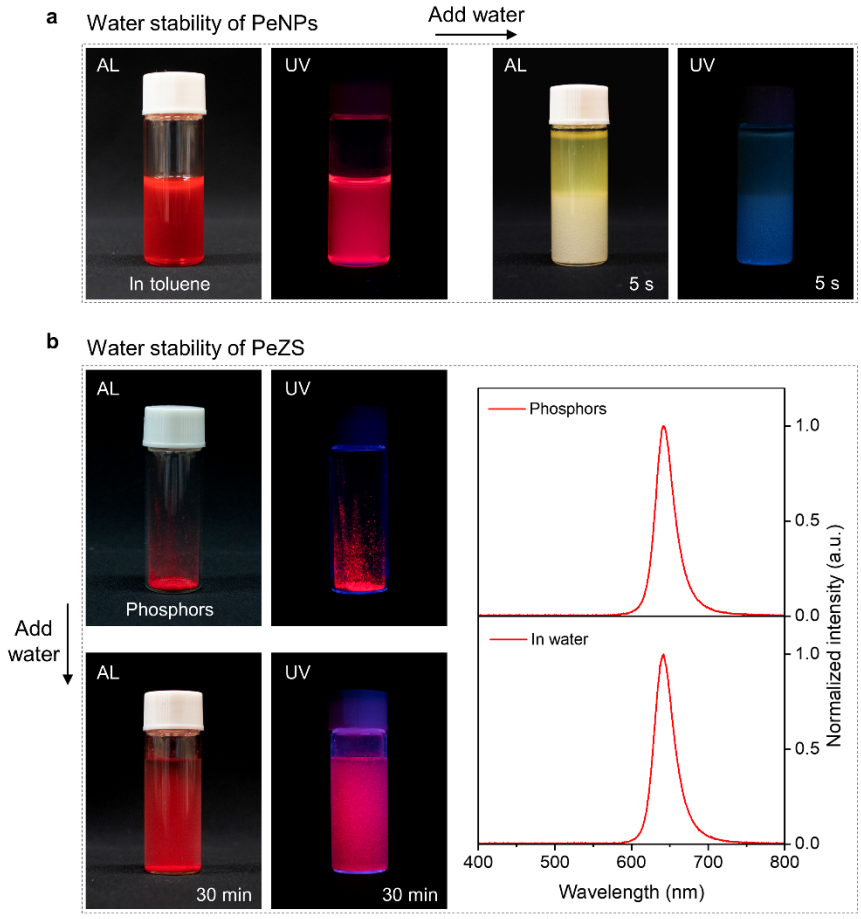


**Supplementary Fig. 15 Water stability assessment.** (a) Stability of PeNPs. Comparative photographs of PeNPs in toluene under ambient light (AL) and UV light conditions, illustrating their initial state and the rapid degradation after introducing water. (b) Stability of PeZS phosphors. Photographs of dried PeZS phosphors and PeZS phosphors immersed in water. The corresponding PL spectra indicate the high water stability of the PeZS phosphors.

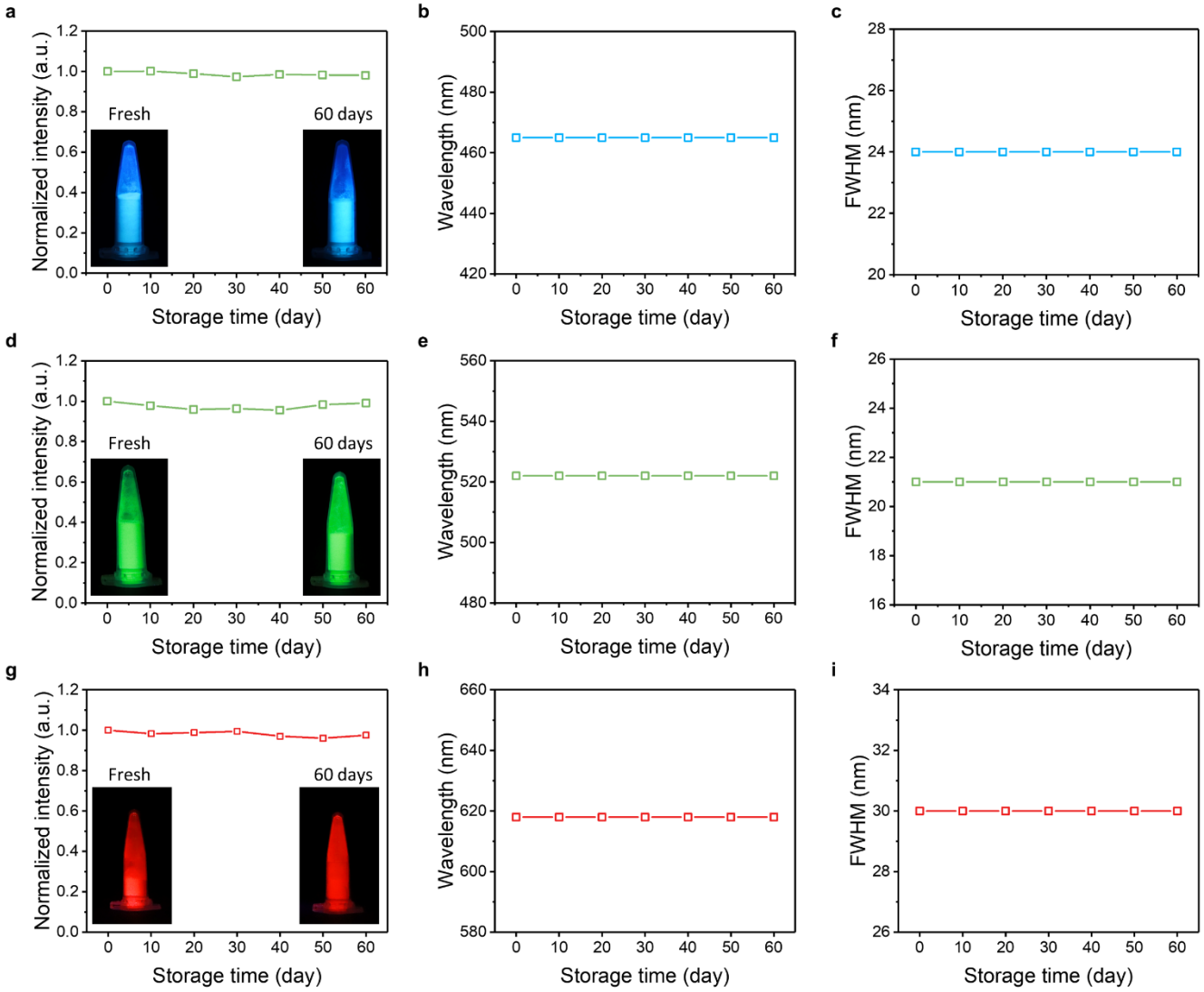


**Supplementary Fig. 16 Stability measurement of PeZS phosphors.** PL intensity, wavelength and FWHM of the blue (a-c), green (d-f) and red (g-i) PeZS phosphors as a function of storage time. Insets show the photographs of the phosphors under UV light.

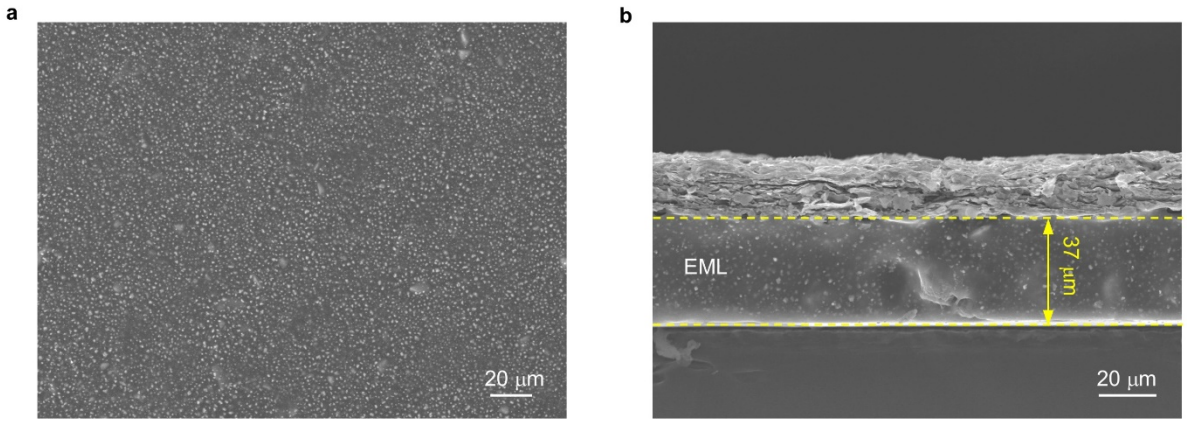


**Supplementary Fig. 17 The microstructure of rigid PeACEL device.** (a) SEM image of the emissive layer. PeZS phosphors and $BaTiO_3$ powders are well dispersed inside the PDMS. (b) Cross-section image of the PeACEL device.

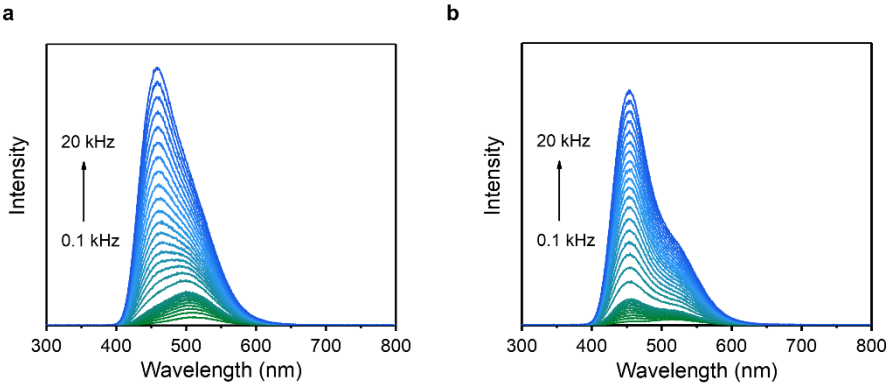


**Supplementary Fig. 18 Characterization of ACEL devices utilizing commercial green and blue ZnS phosphors operating at 100 V.** EL spectra of green (a) and blue (b) ACEL devices at various AC operating frequencies.

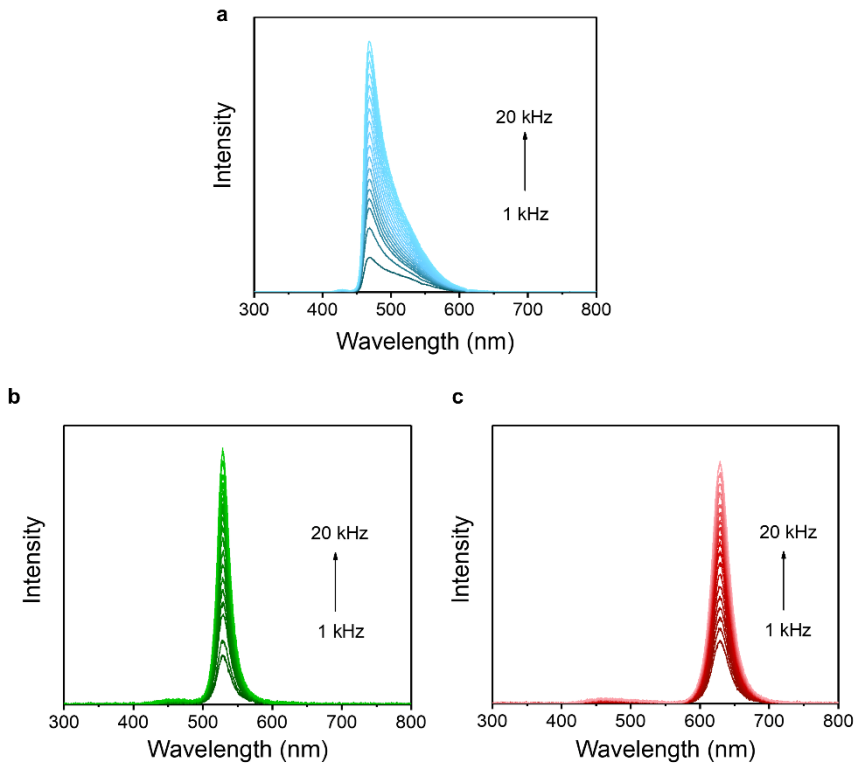


**Supplementary Fig. 19 Characterization of PeACEL devices operating at 100 V.** (a-c) EL spectra of blue-, green- and red-emitting PeACEL devices operating at different AC frequencies, respectively.

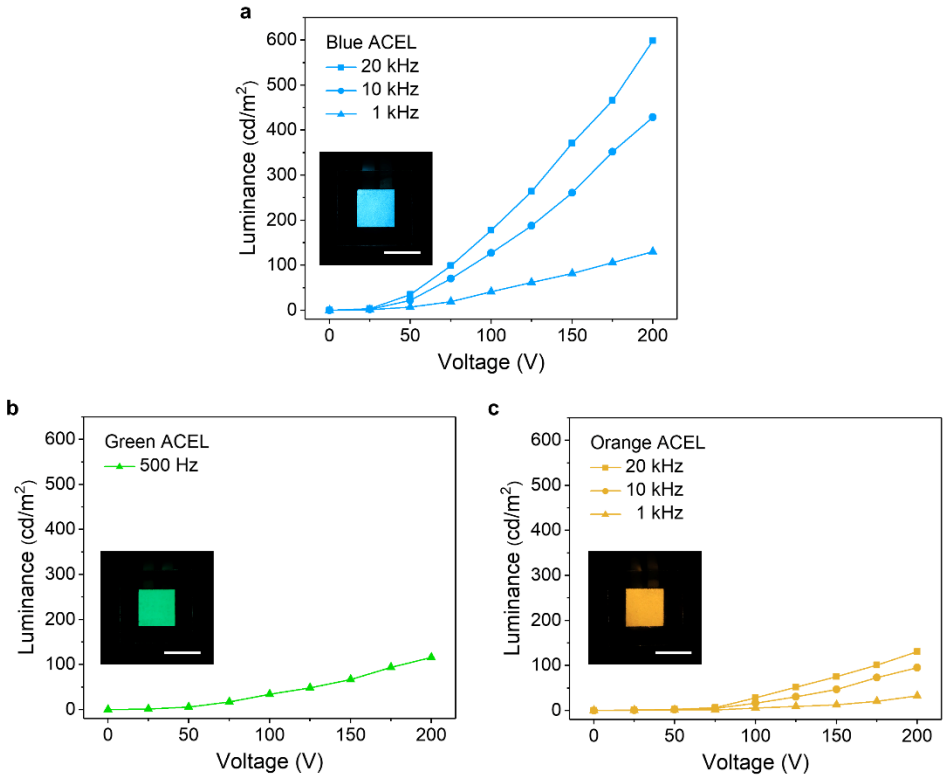


**Supplementary Fig. 20 EL properties of the ACEL device using commercial EL phosphors.** (a-c) Luminance–voltage characteristic of the blue, green and orange devices, respectively. Insets present EL images. Scale bars, 1 cm. It is noteworthy that elevated frequencies engender a blue shift in green ACEL, confining the applied frequencies to only 500 Hz.

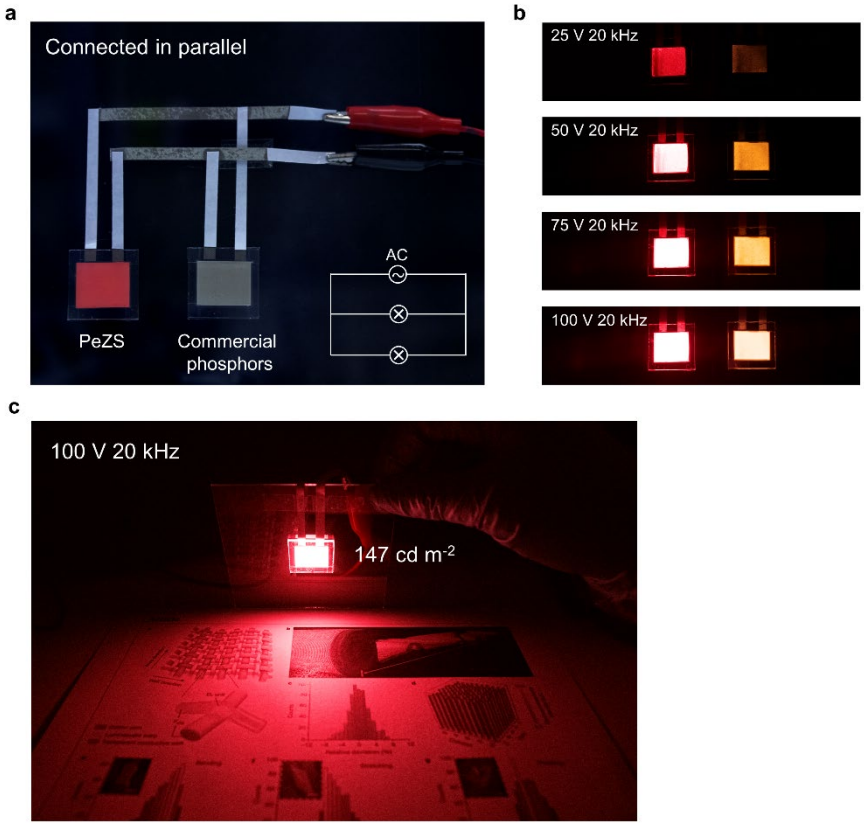


**Supplementary Fig. 21 EL properties of red PeZS phosphors and commercial orange ZnS:Mn phosphors.** (a) Photograph of EL devices fabricated with PeZS phosphors and commercial ZnS:Mn phosphors connected in parallel. (b) Photographs of these EL devices operating at a working voltage of 25, 50, 75 and 100 V, respectively. (c) Photograph of a white reference paper illuminated by an operating PeACEL device excited at 100 V and 20 kHz.

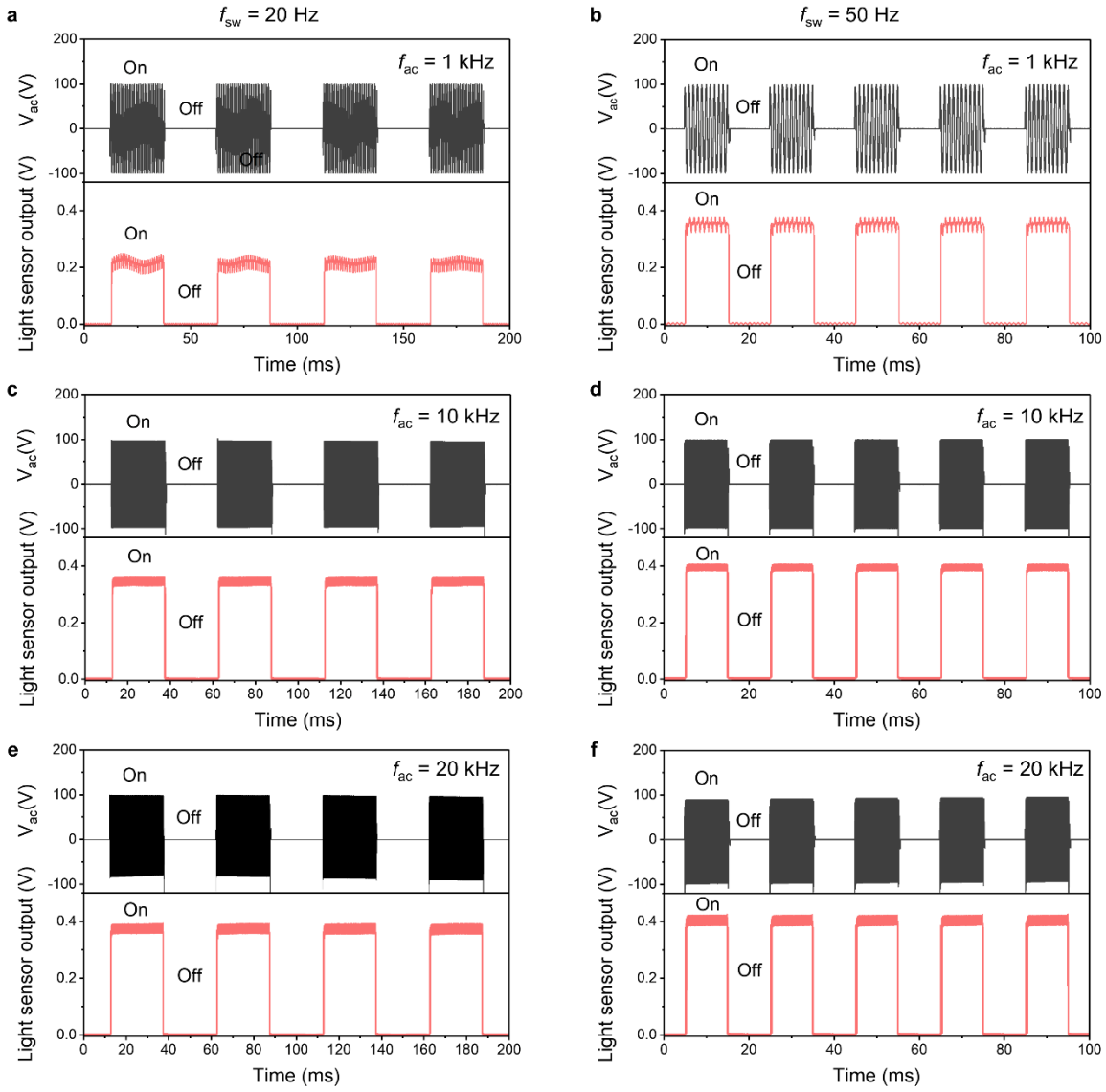


**Supplementary Fig. 22 Characterization of light signals detected by a photodiode from a red-emitting PeACEL device operating at 100 V.** The device operates at switching frequencies ($f_{sw}$) of 20 and 50 Hz, while the alternating current frequencies ($f_{ac}$) vary at 1, 10, and 20 kHz. (a-f) Light signal follows turn-on and turn-off cycles under various combinations of $f_{ac}$ and $f_{sw}$.

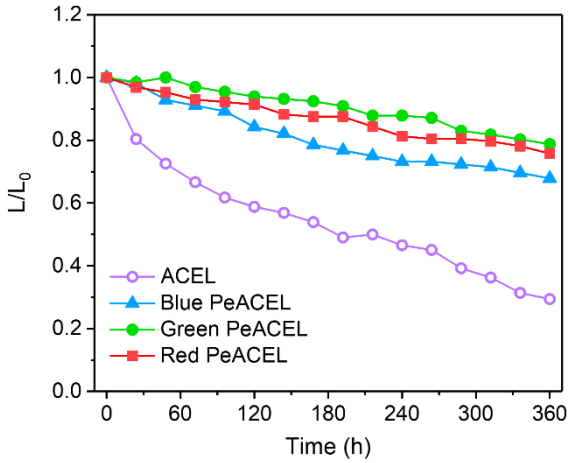


**Supplementary Fig. 23 Continuous operating stability of an ACEL device based on uncoated ZnS phosphors, as well as blue, green, and red PeACEL devices, all at 20 kHz and 100 V.**

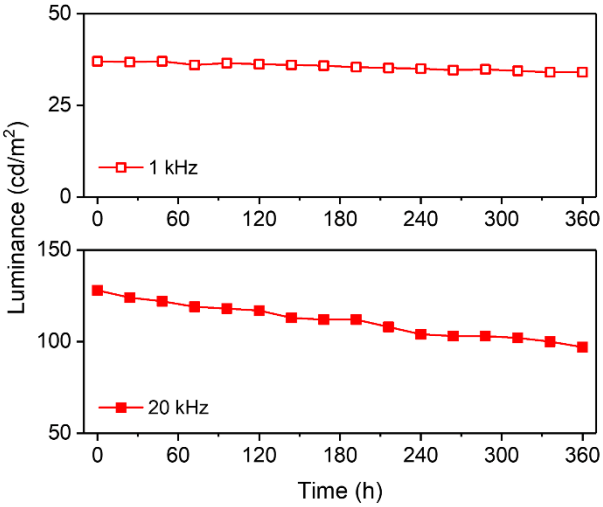


**Supplementary Fig. 24 Continuous operating stability of the red PeACEL devices at 100 V across various frequencies.**

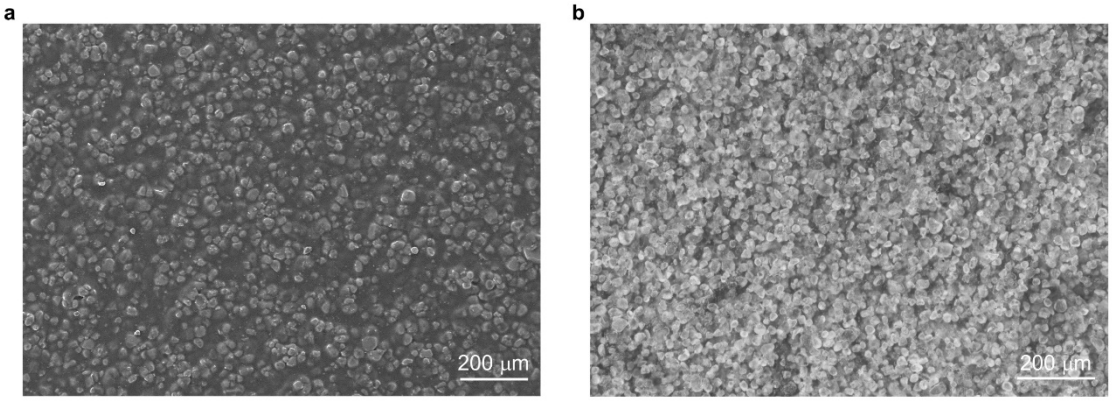


**Supplementary Fig. 25 Micromorphology of the EML consisting of red PeZS phosphors and SEBS matrix.** (a) SEM image. (b) Optical microscopy image.

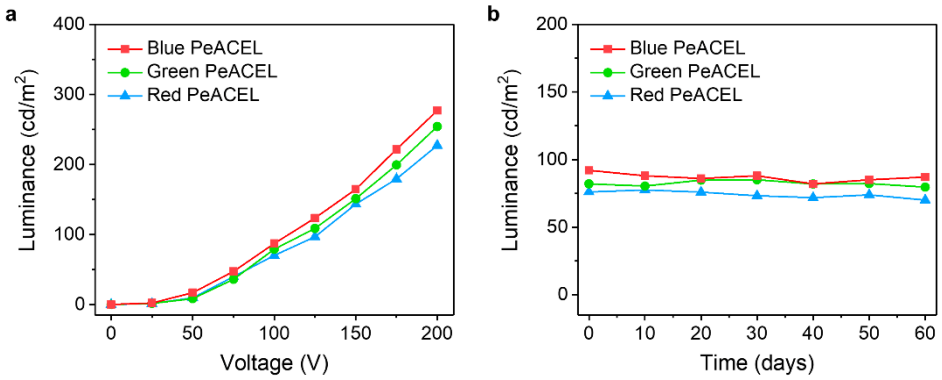


**Supplementary Fig. 26 EL properties of flexible PeACEL devices.** (a) The luminance of the devices operating at $f_{ac}$=20 kHz, with varying voltage. (b) Storage stability test of the devices at 100 V, 20 kHz.

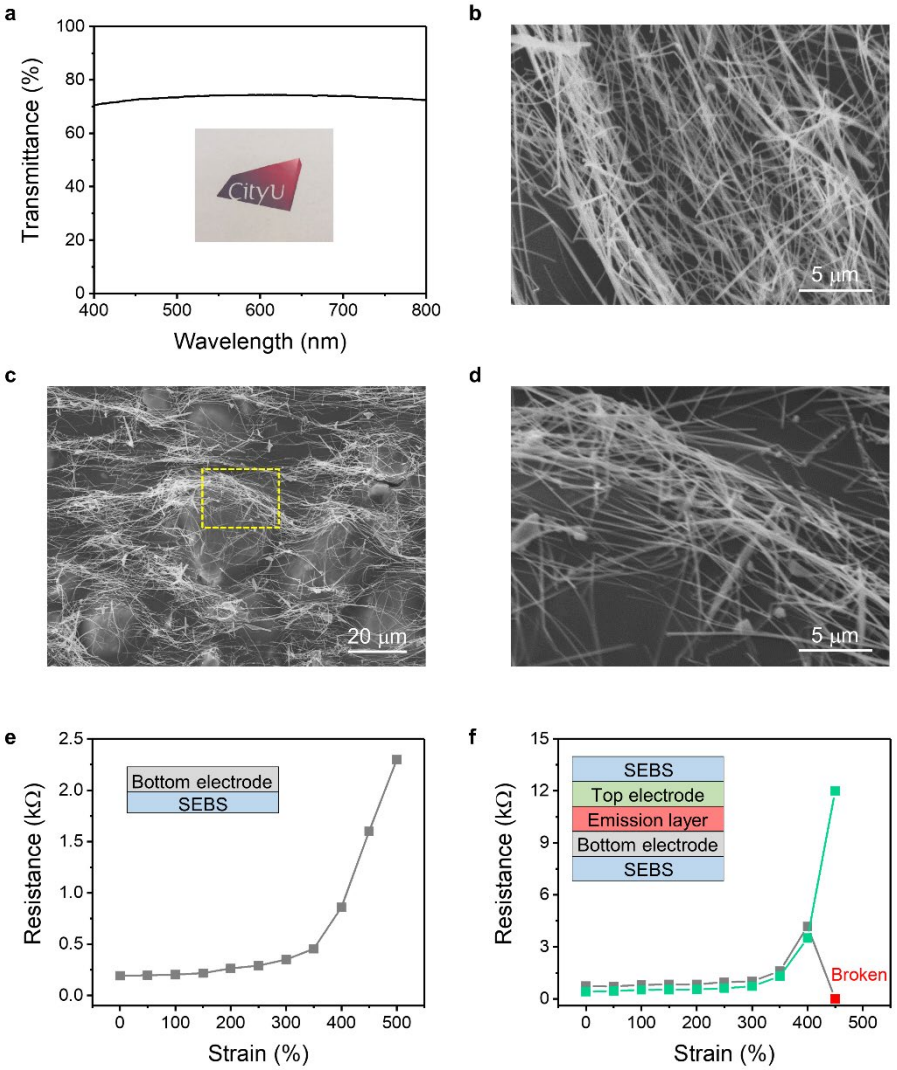


**Supplementary Fig. 27 Evaluation of AgNWs electrode.** (a) Transmittance spectrum of the bottom electrode (SEBS/AgNWs) in the visible range. Inset shows an optical image of the bottom electrode affixed to patterned paper. (b) SEM image of the bottom electrode (SEBS/AgNWs). (c, d) Low-magnification and magnified SEM images of top electrode (SEBS/AgNWs/EML/AgNWs). (e) Resistance variation of the bottom electrode (SEBS/AgNWs) under various strains. (f) Resistance alteration in the bottom and top electrodes (in encapsulated devices) under various strains.

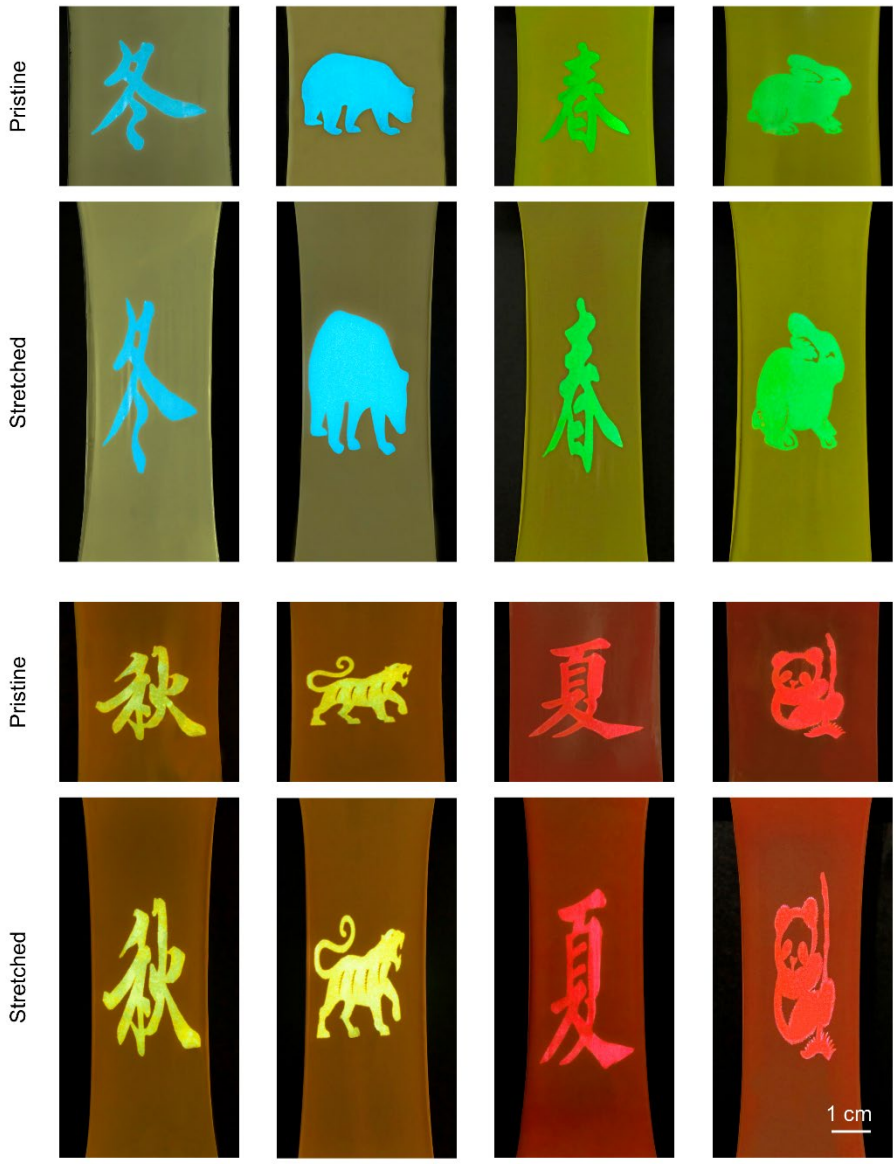


**Supplementary Fig. 28 Patterned multicolour PeACEL devices under pristine and stretched conditions.** Photographs showing the PeACEL devices operating at 100 V with an $f_{ac}$ of 20 kHz under daylight conditions.

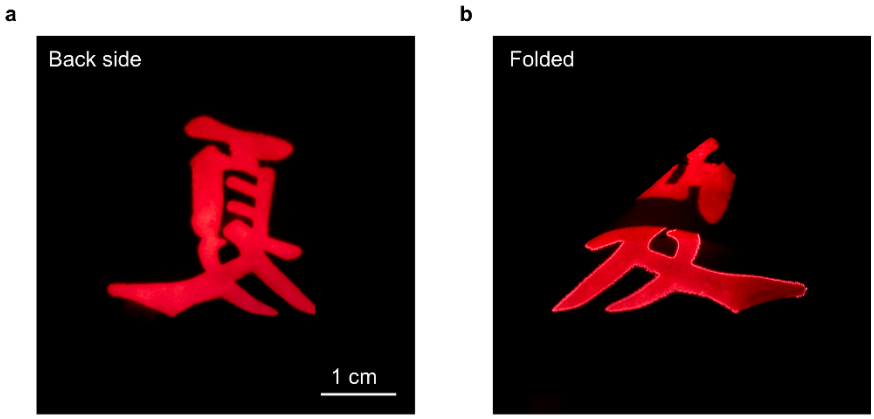


**Supplementary Fig. 29 EL images of the flexible patterned PeACEL device.** (a) The back side view of the operating device. (b) The optical image of the device operated under a folded state.

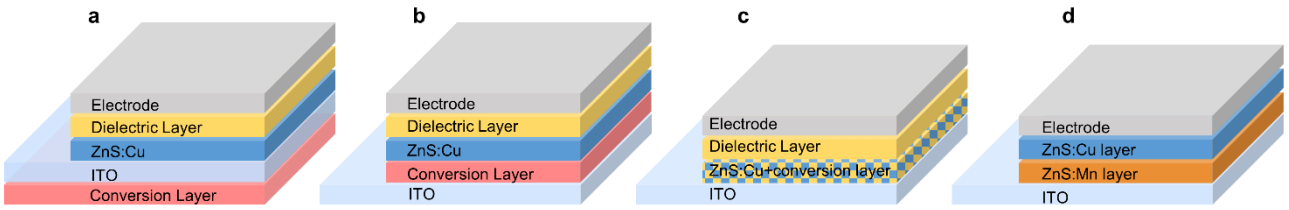


| Structure | a | b | c | d | This work |
|---|---|---|---|---|---|
| Materials | ZnS:Cu, PeNP | ZnS:Cu, phosphors<br>ZnS:Cu, PeNP | ZnS:Cu, YAG:Ce | ZnS:Cu, ZnS:Mn | PeZS phorsphors |
| Color range | Green, white | Blue → white<br>Blue → green | Blue → white | Orange → blue | Blue → deep red |
| Color purity | high | low | low | low | high |
| Flexibility | Flexible | Rigid, Flexible | Rigid, flexible | flexible | flexible |
| Stretchability | 180% | No | 150% | No | 400% |
| Reference | 22,23 | 24,25 | 26,21 | 18 | |

**Supplementary Fig. 30 Comparison of the current multicolour ACEL using colour conversion layer.**

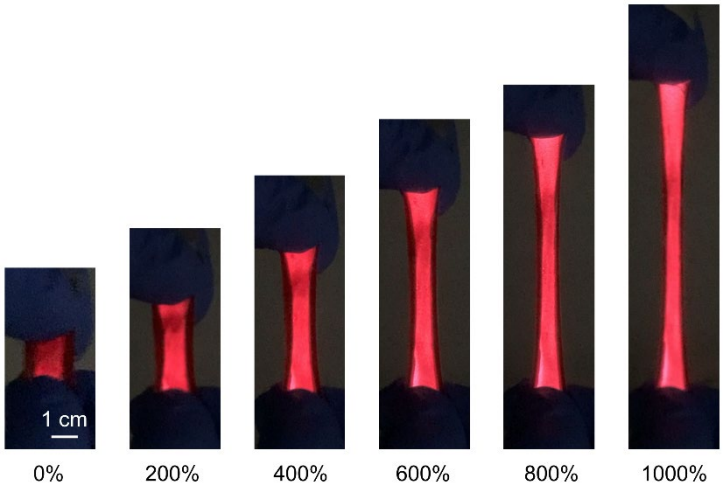


**Supplementary Fig. 31 The stretchable performance of the red-emitting PeACEL device with SEBS as matrix and hydrogel as electrodes, operating at 100 V and 10 kHz.**

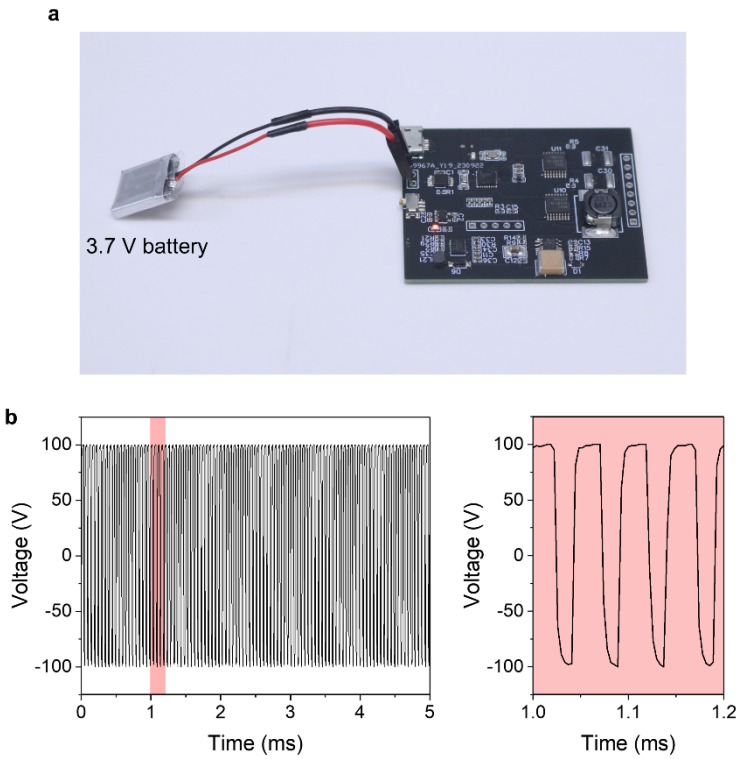


**Supplementary Fig. 32 The driver unit.** (a) Photograph. (b) Output.

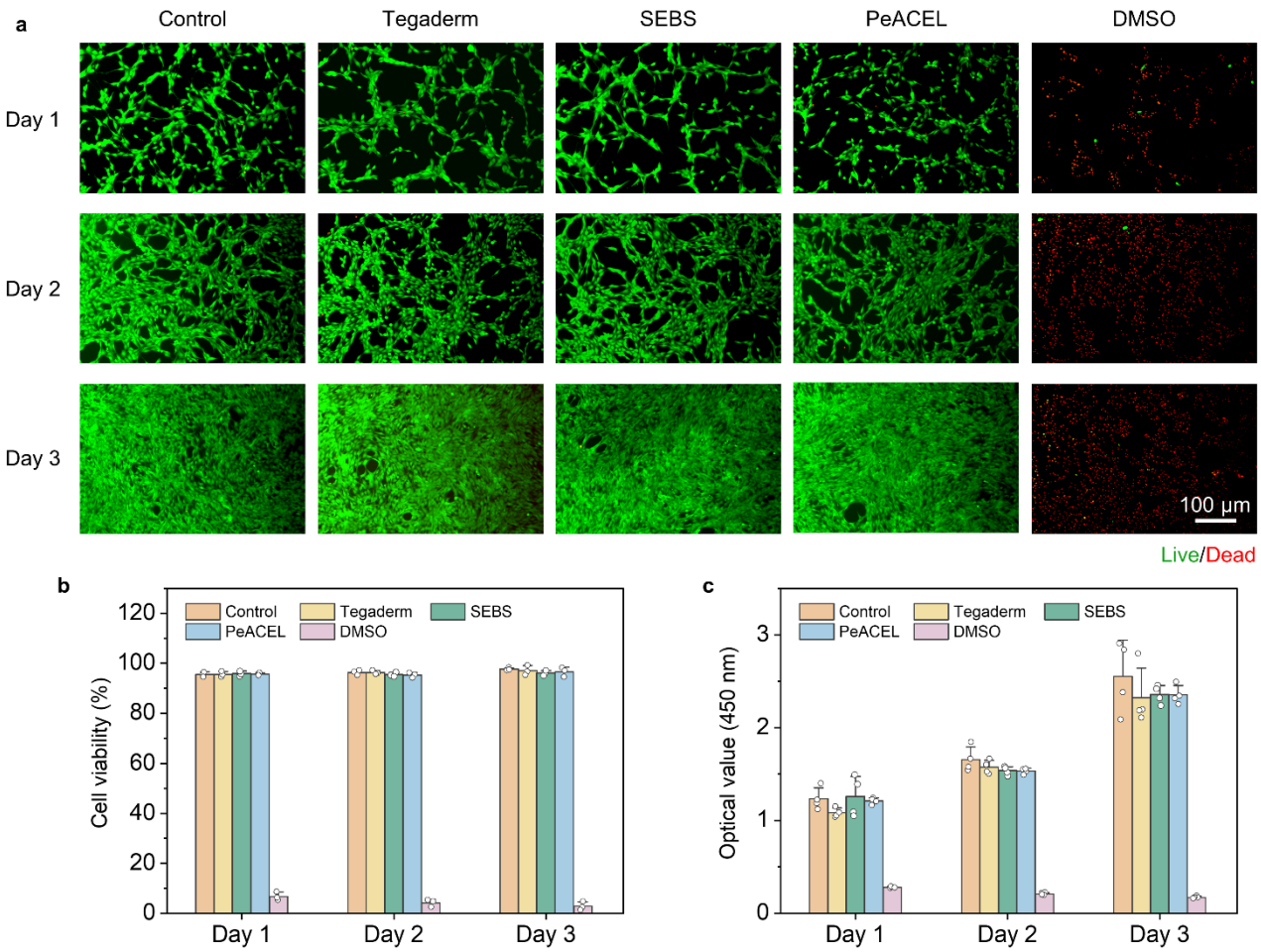


**Supplementary Fig. 33 Biocompatibility of PeACEL devices.** (a) Fluorescence images of cells cultured in the incubation medium with the control sample, 3M Tegaderm dressing, SEBS, PeACEL device and DMSO. (b) Cell viability in different incubation groups. Bar height, mean; error bars, s.d.; n = 3 independent samples. (c) Optical density of various groups after 1, 2 and 3 days of incubation. Bar height, mean; error bars, s.d.; n = 4 independent samples.

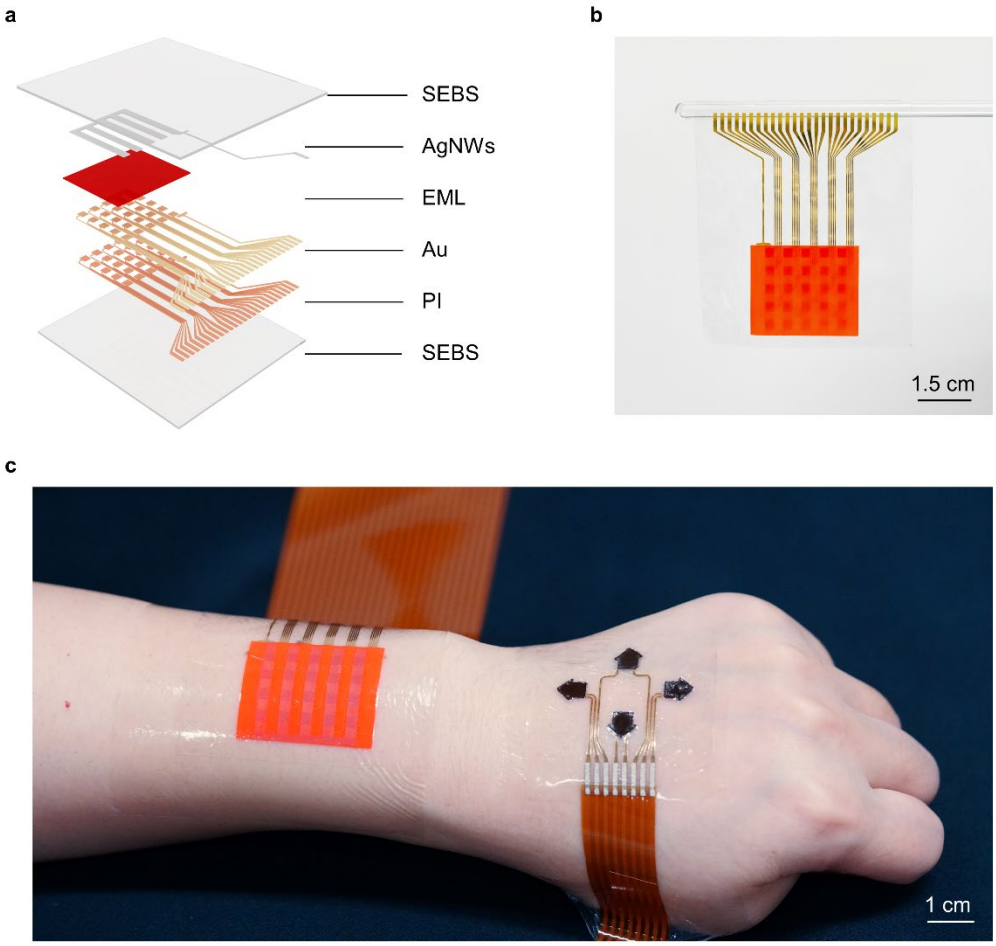


**Supplementary Fig. 34 Red-emitting PeACEL array.** (a) Exploded schematics of the PeACEL array. The multilayer structure comprises SEBS, PI, Au, EML, AgNWs, and SEBS. (b) Photograph of the PeACEL array. (c) PeACEL array and tactile sensor applied to human skin.

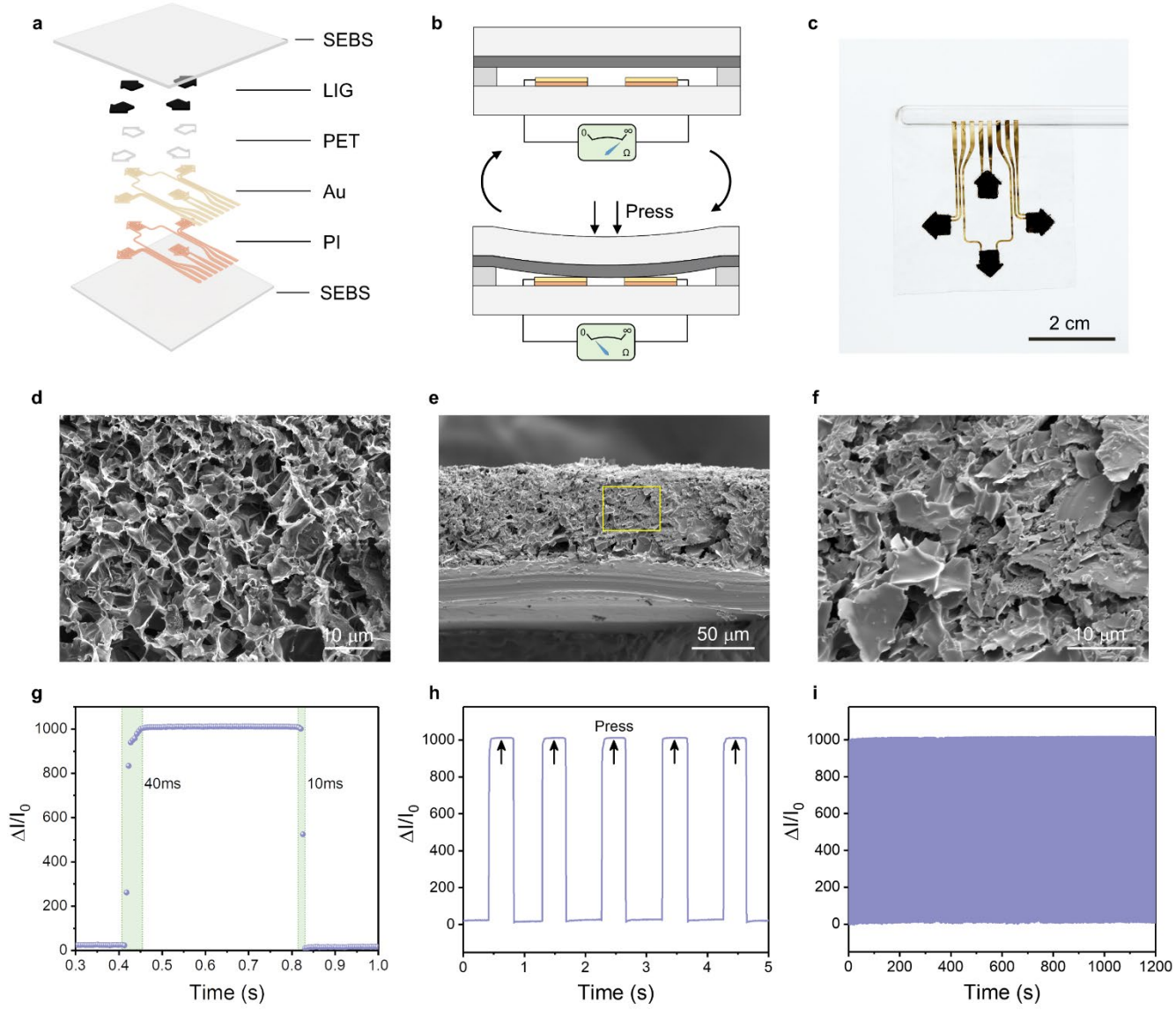


**Supplementary Fig. 35 Characterization of tactile sensor.** (a) Exploded schematics of the tactile sensor. The multilayer structure contains SEBS, PI, Au, PET, LIG, and SEBS. (b) Mechanism of the tactile sensor. (c) Photograph of the tactile sensor. (d) SEM image of the LIG electrode. (e, f) Cross-section view and the magnification of LIG. (g) Response and recovery time of the tactile sensor. (h) Pressing responses with human finger touch. (i) Repeatability measurement for 500 cycles.

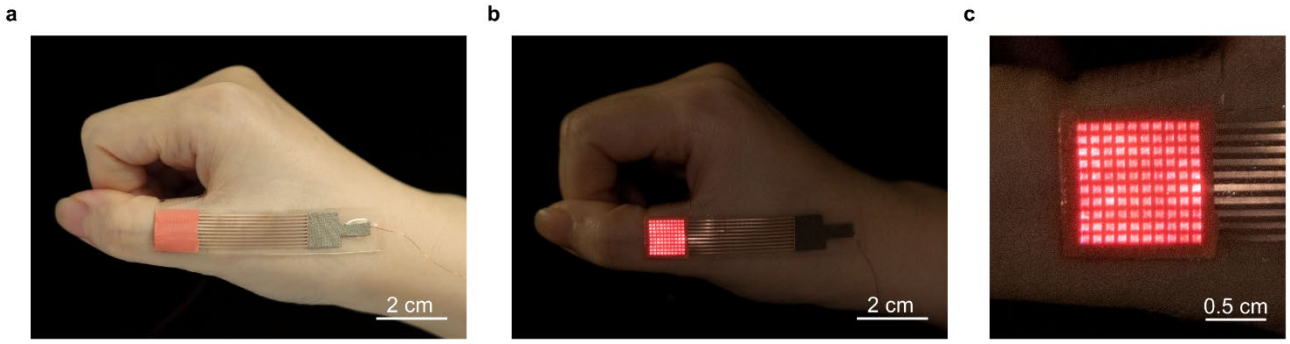


**Supplementary Fig. 36 Photographs of the wearable (10×10) PeACEL arrays laminated on a finger.** (a) Optical image under ambient light. (b) Optical image of the arrays operating at 100 V with an $f_{ac}$ of 20 kHz. (c) Enlarged image of the operational PeACEL arrays.

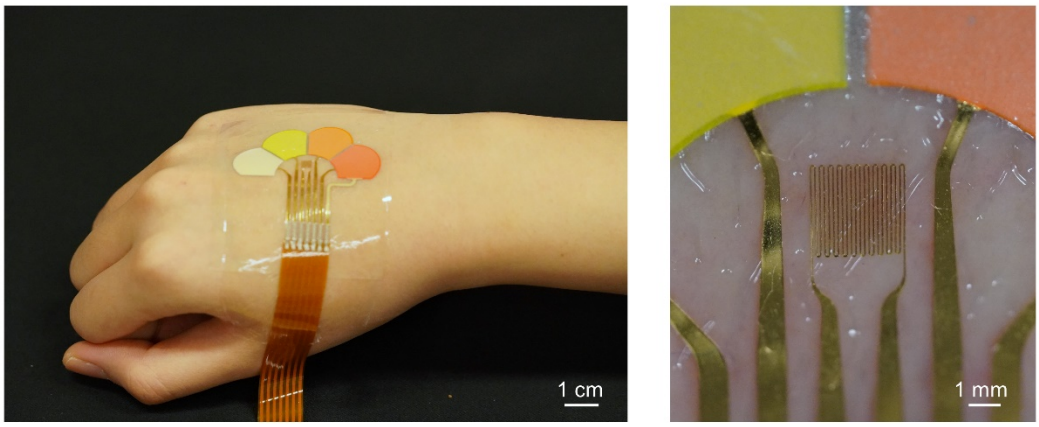


**Supplementary Fig. 37 Optical images showing the visual temperature sensing film affixed on the hand with a magnified view of the temperature sensor.**

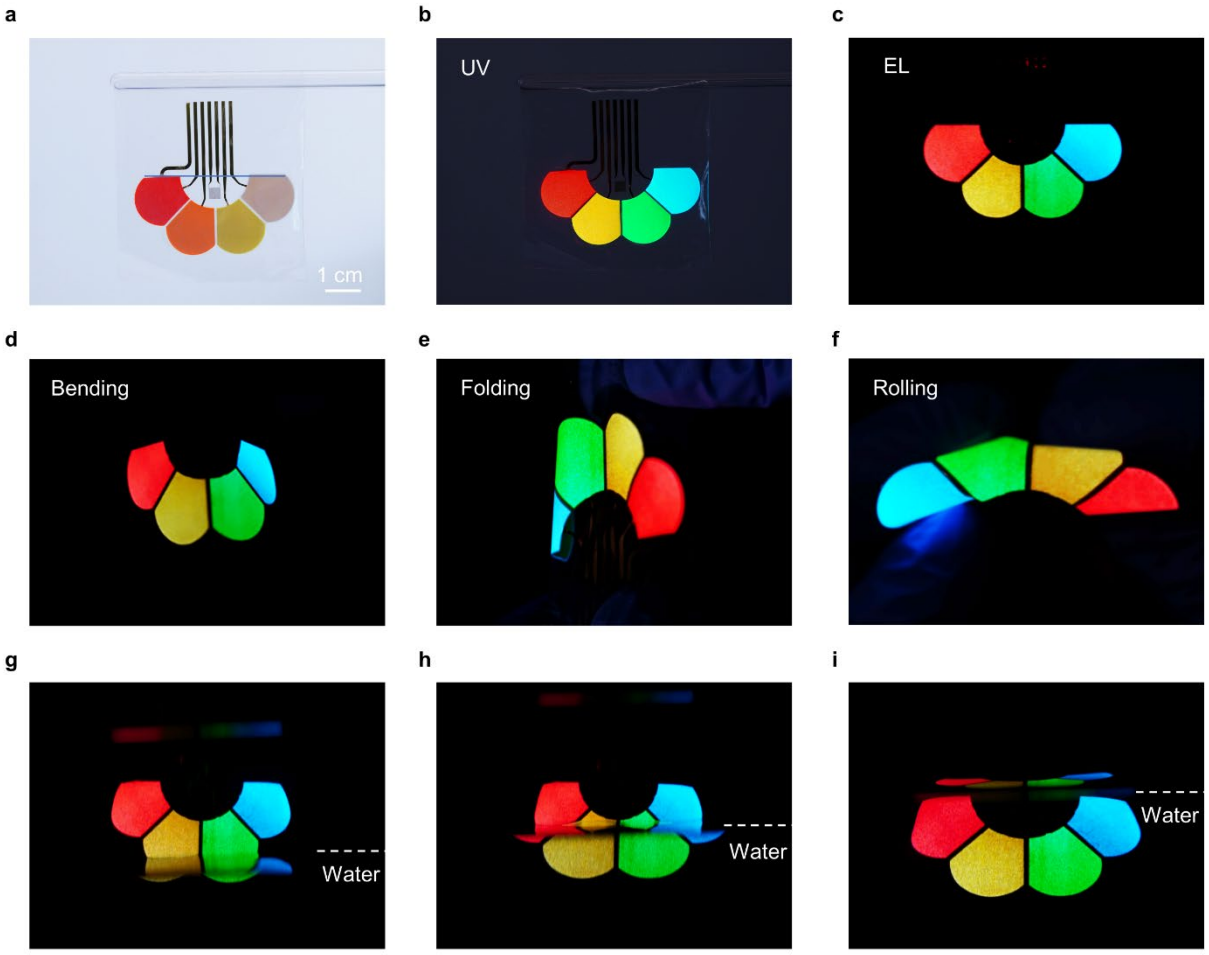


**Supplementary Fig. 38 Optical images of the visual temperature sensor.** (a) Optical image under ambient light. (b) Optical image under UV light. (c) Optical image of the visual temperature sensor operated without deformation. (d-f) Optical images of the visual temperature sensor operated under bending, folding, and rolling. (g-i) Optical images of the operated visual temperature sensor placed at various water levels.

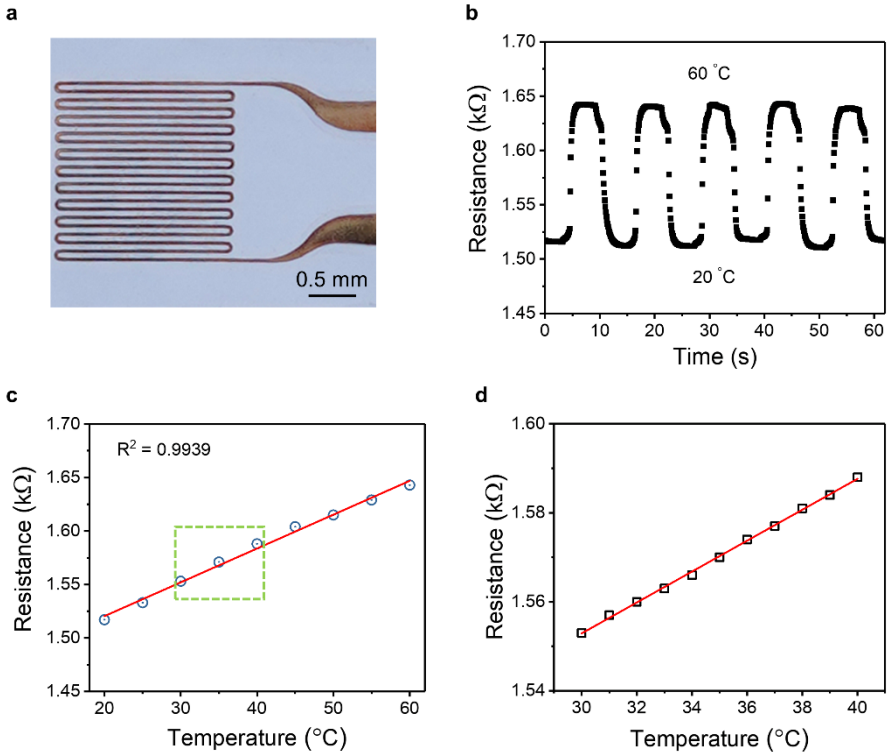


**Supplementary Fig. 39 Characterization of the temperature sensor.** (a) An optical image of the temperature sensor. (b) Reversibility of resistance changes at different temperatures (20 °C and 60 °C). (c) Temperature-dependent resistance ranges from 20 to 60 °C with a resolution of 10 °C. (d) Temperature-dependent resistance ranges from 30 to 40 °C with a resolution of 1 °C.

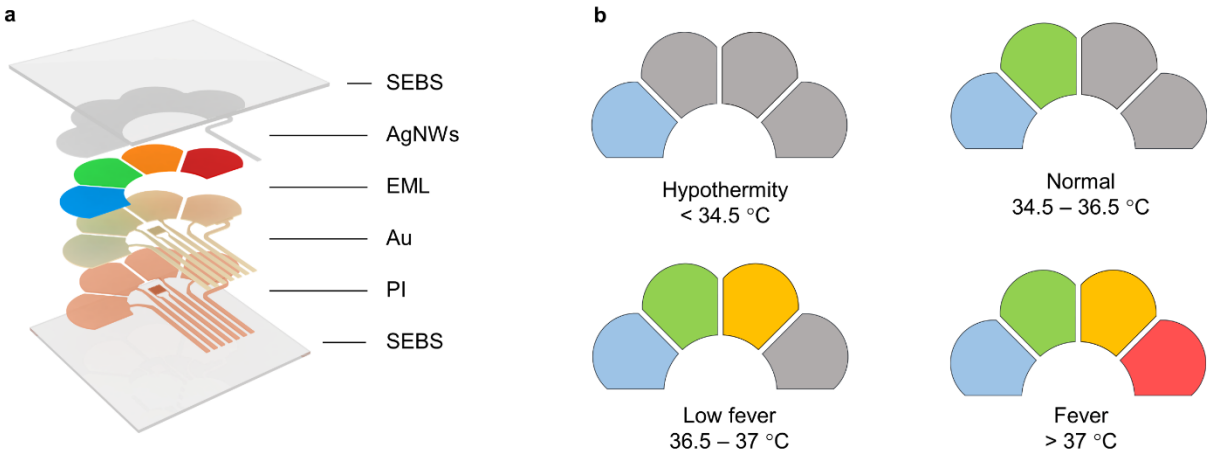


**Supplementary Fig. 40 Design of the visual temperature sensor.** (a) Exploded schematics of the device. The multilayer structure contains SEBS, PI, Au, EML, AgNWs, and SEBS. (b) Demonstration of various display patterns. Hypothermia is defined as the measured temperature below 34.5 °C, normal temperature between 34.5 and 36.5 °C, low fever between 36.5 and 37 °C, and fever temperature greater than 37 °C.

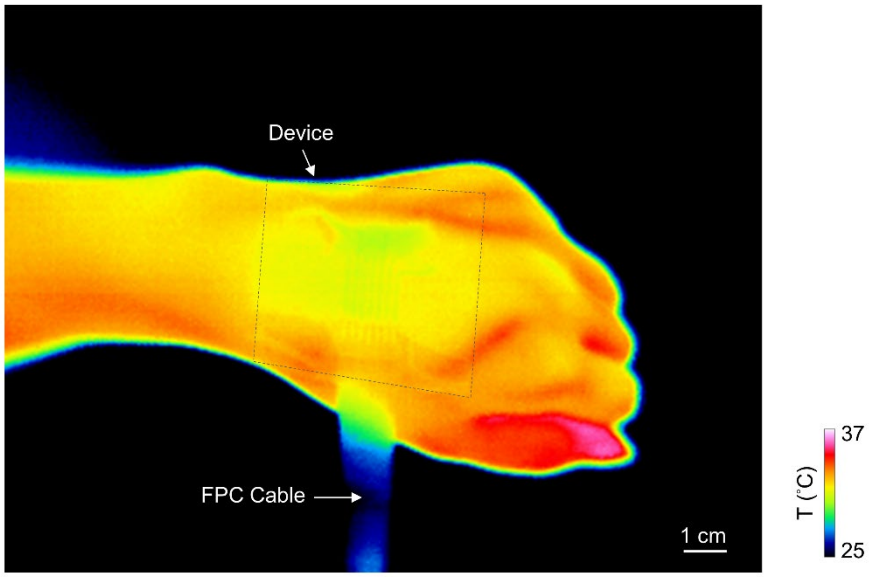


**Supplementary Fig. 41 Thermal image of the visual temperature sensor mounted on the hand under normal operating conditions.** The dashed box indicates the position of the device. T stands for the temperature.

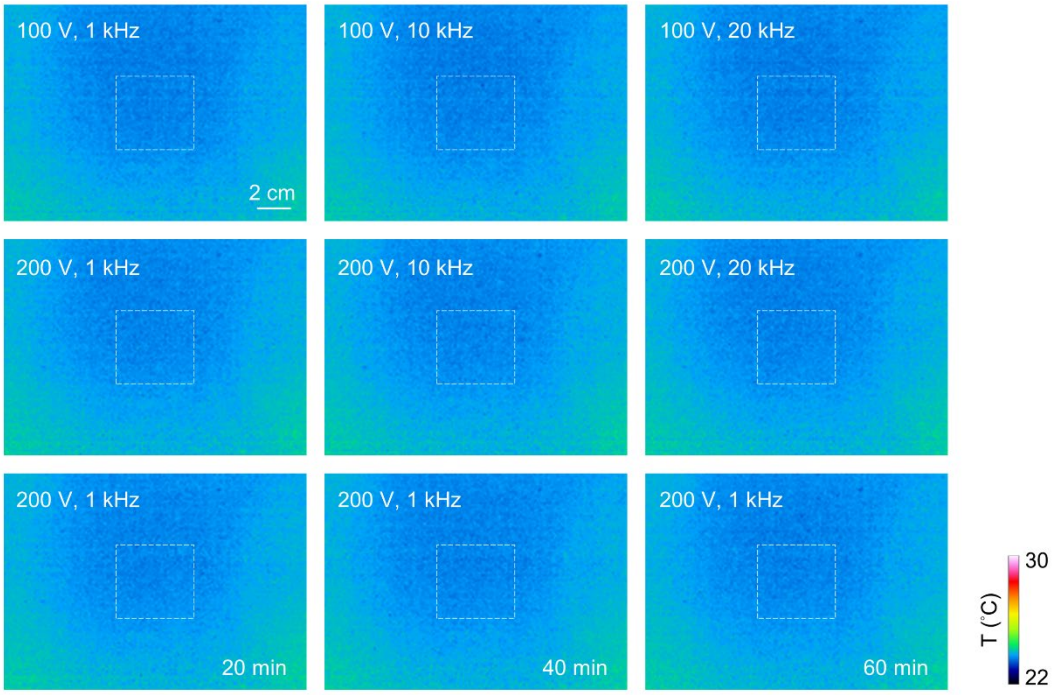


**Supplementary Fig. 42 Thermal images of the visual temperature sensor operated at different frequencies, voltages, and durations.** The white dashed box indicates the position of the device. T stands for the temperature.

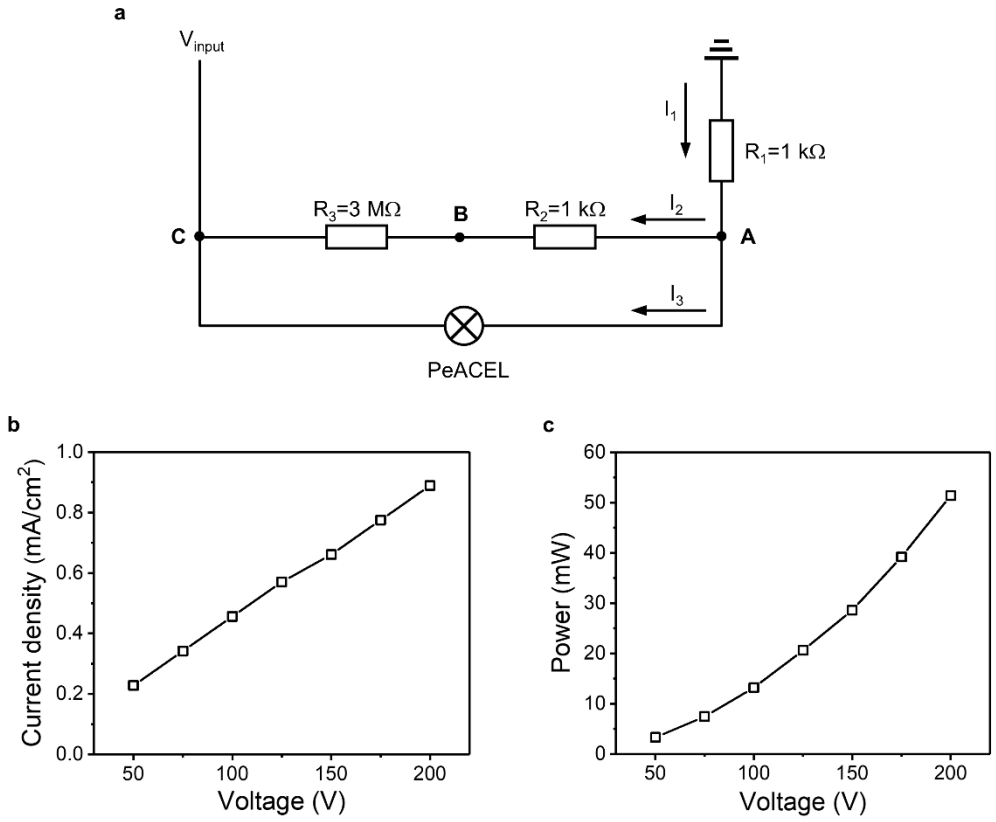


**Supplementary Fig. 43 Electroluminescence performance of the PeACEL unit (red-emitting petal of the visual temperature sensor).** (a) Test circuit for measurement of power consumption of the PeACEL unit. (b) Current density–voltage of the PeACEL unit. (c) Power–voltage of the PeACEL unit.

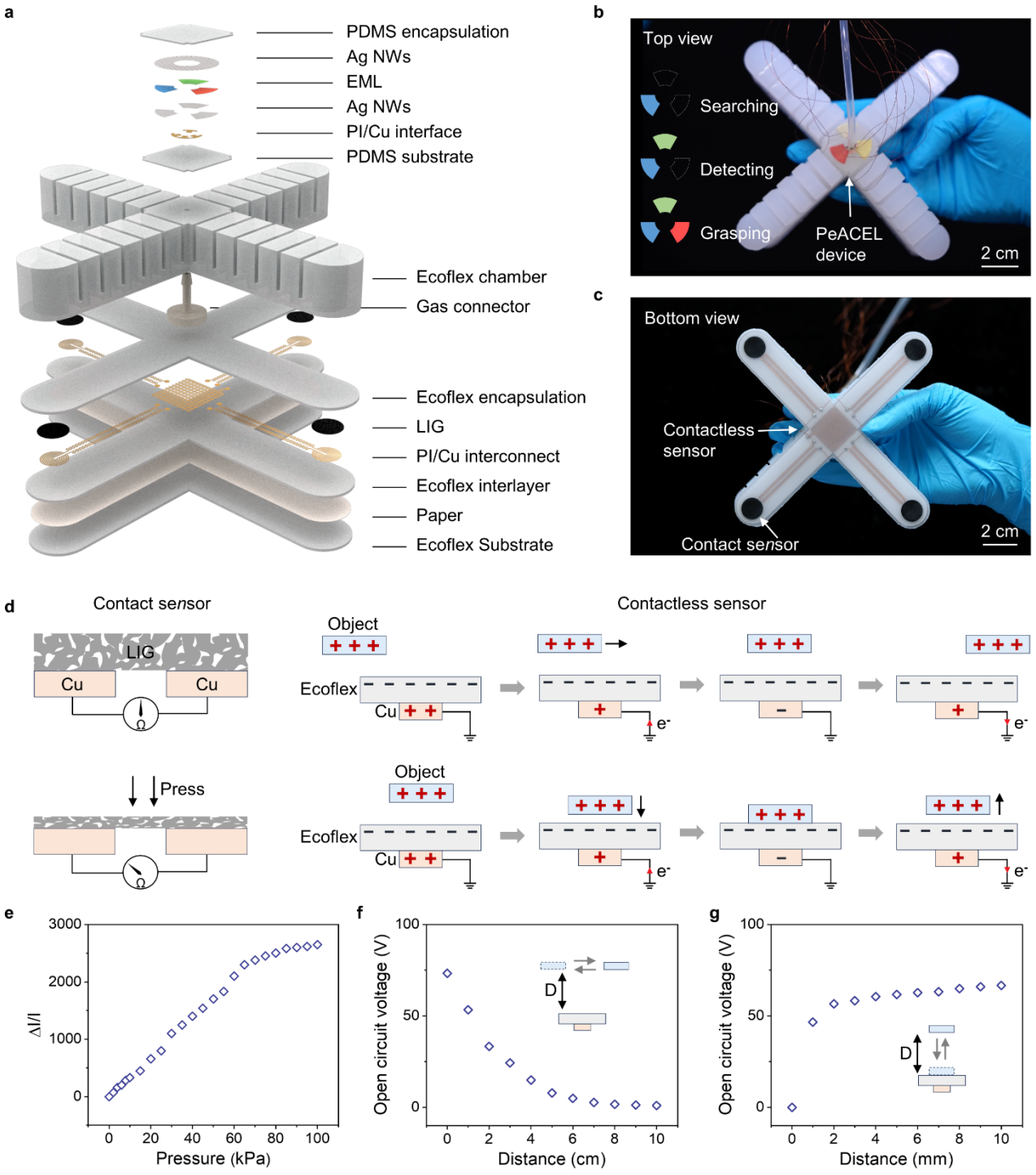


**Supplementary Fig. 44 Sensing visualization in a soft robotic system.** (a) Exploded view of the soft robots equipped with patterned PeACEL. (b) Photograph showing the top view of the soft robots fitted with the PeACEL device. The inset shows varying display status of PeACEL during searching, detecting and grasping phases. (c) Photograph illustrating the bottom view of the soft robots, equipped with contact and contactless sensors. (d) Sensing mechanism schematic of the prototype. The contact sensor is based on the piezoresistive effect, while the contactless sensor is predicated on the triboelectrification effect. (e) Currents corresponding to the LIG-based sensor fluctuate with increasing pressure. (f, g) Output voltage of the contactless sensor as the object moves in horizontal and vertical directions, respectively.

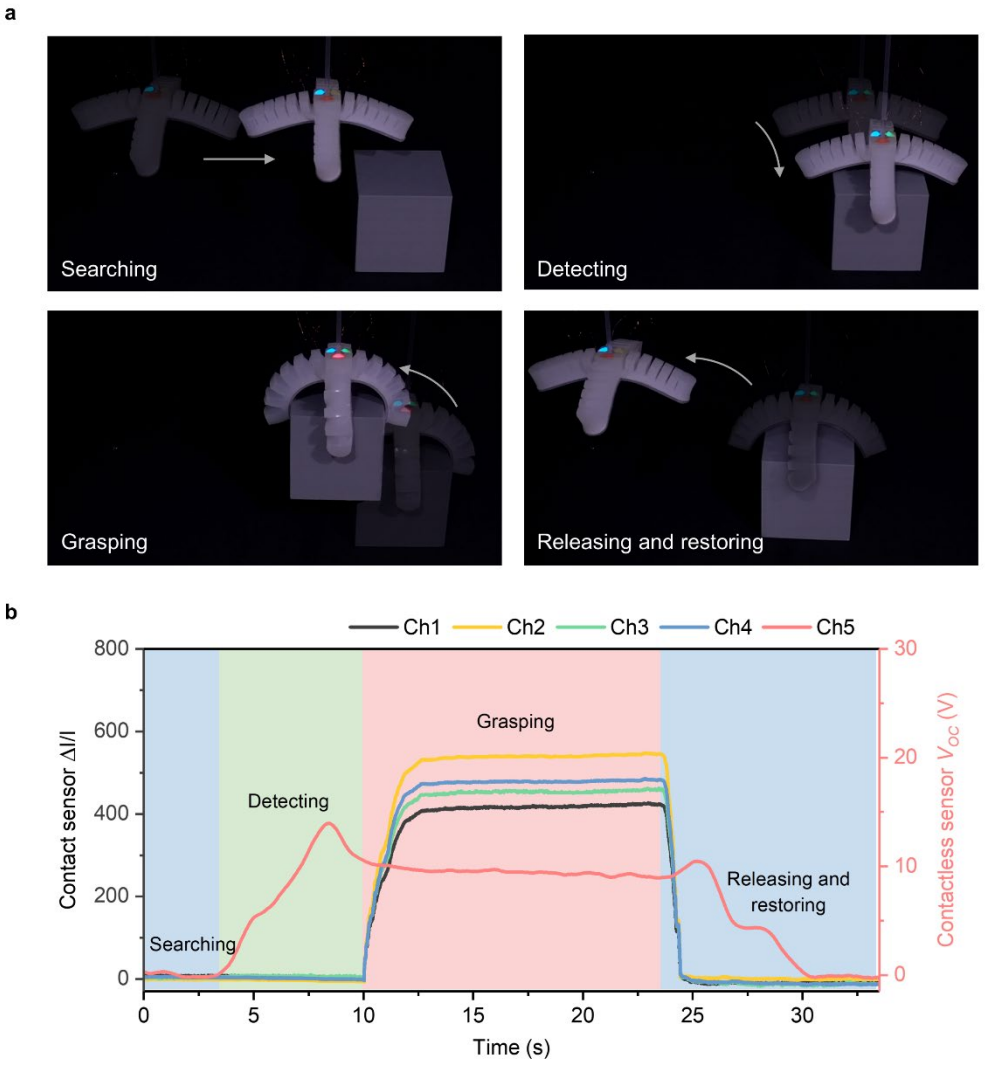


**Supplementary Fig. 45 Demonstration of the PeACEL-integrated soft gripper approaching, grasping and releasing a 3D-printed cube object.** (a) Various display patterns indicating the soft gripper under searching, detecting, grasping, releasing and restoring states. (b) Real-time outputs of the contact (channels 1-4) and contactless (channel 5) sensors during the motion.

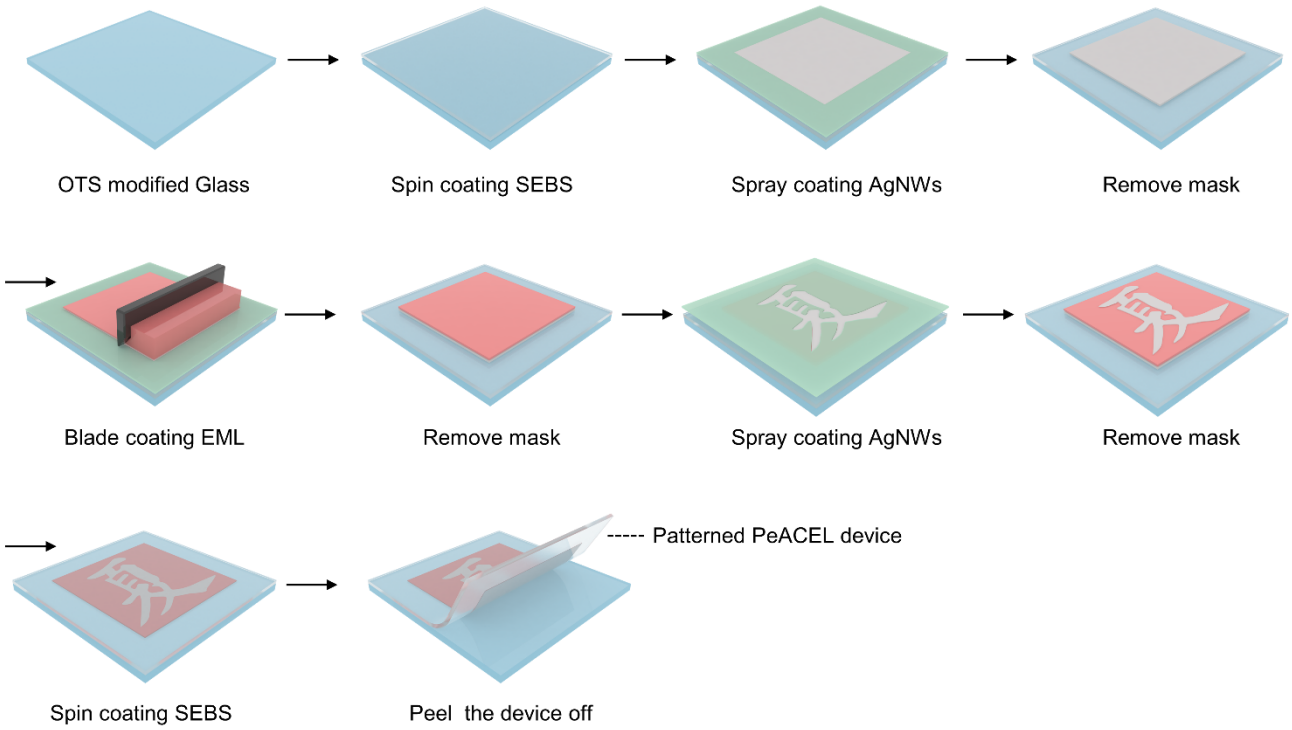


**Supplementary Fig. 46 The detailed fabrication process of patterned PeACEL device.**

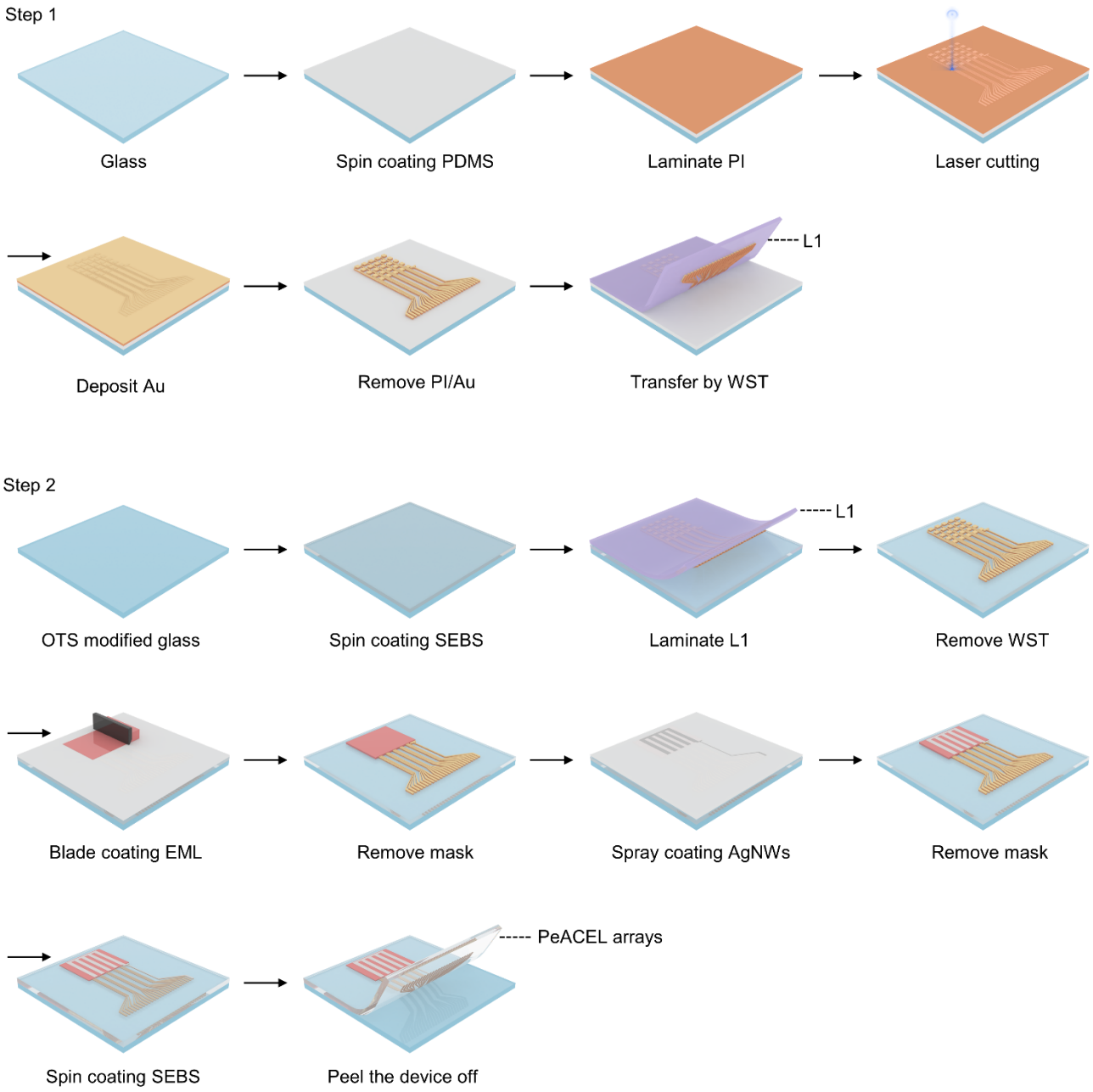


**Supplementary Fig. 47 The detailed fabrication process of red-emitting PeACEL arrays.**

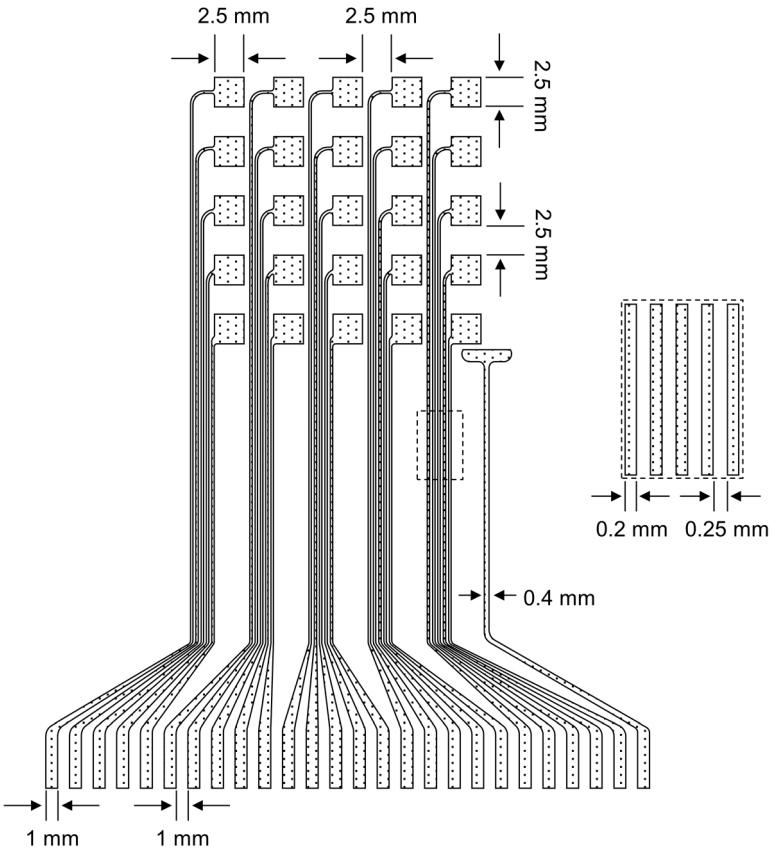


**Supplementary Fig. 48 Mechanical pattern design of the bottom electrodes of PeACEL array.**

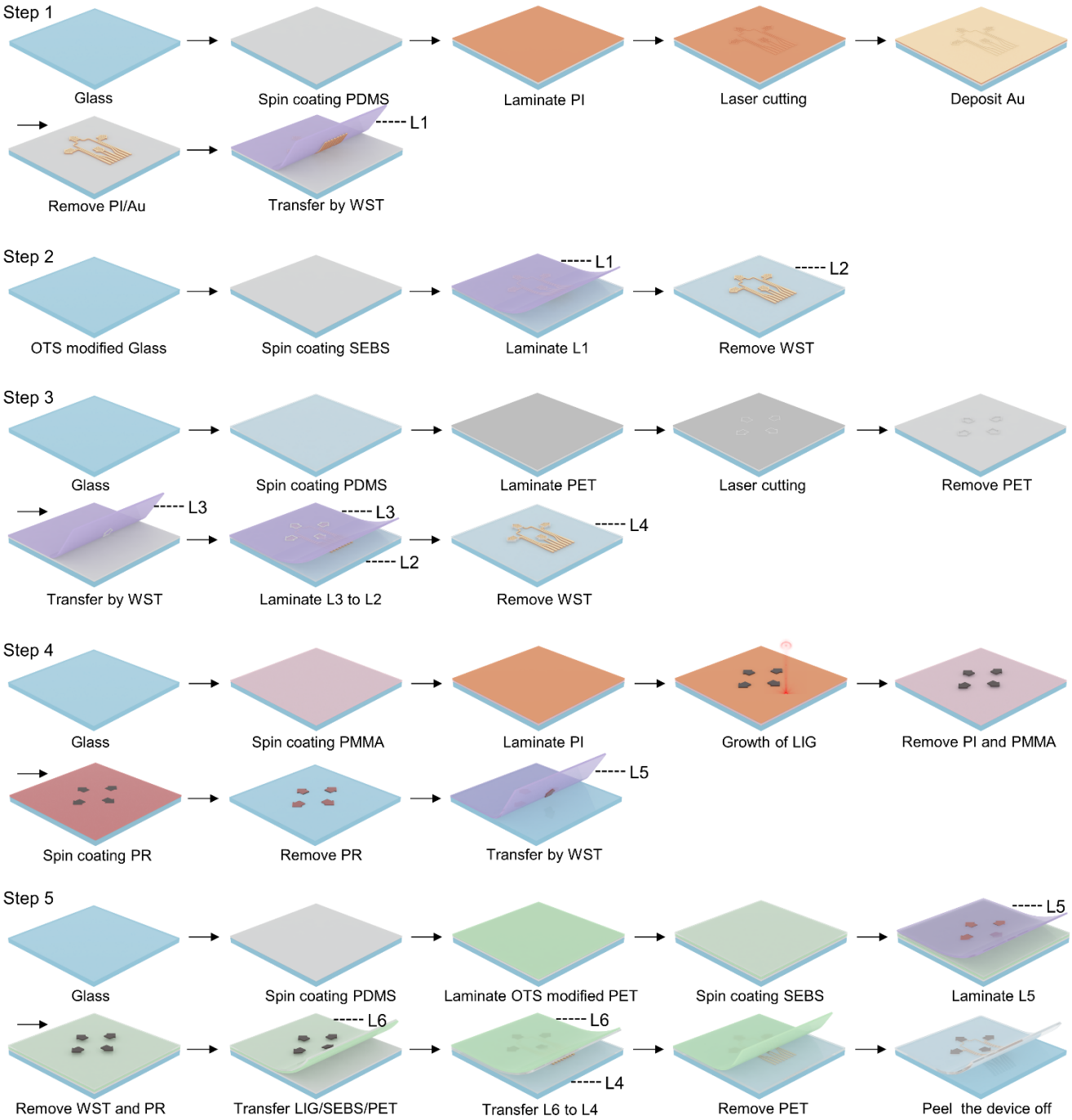


**Supplementary Fig. 49 The detailed fabrication process of the tactile sensor.**

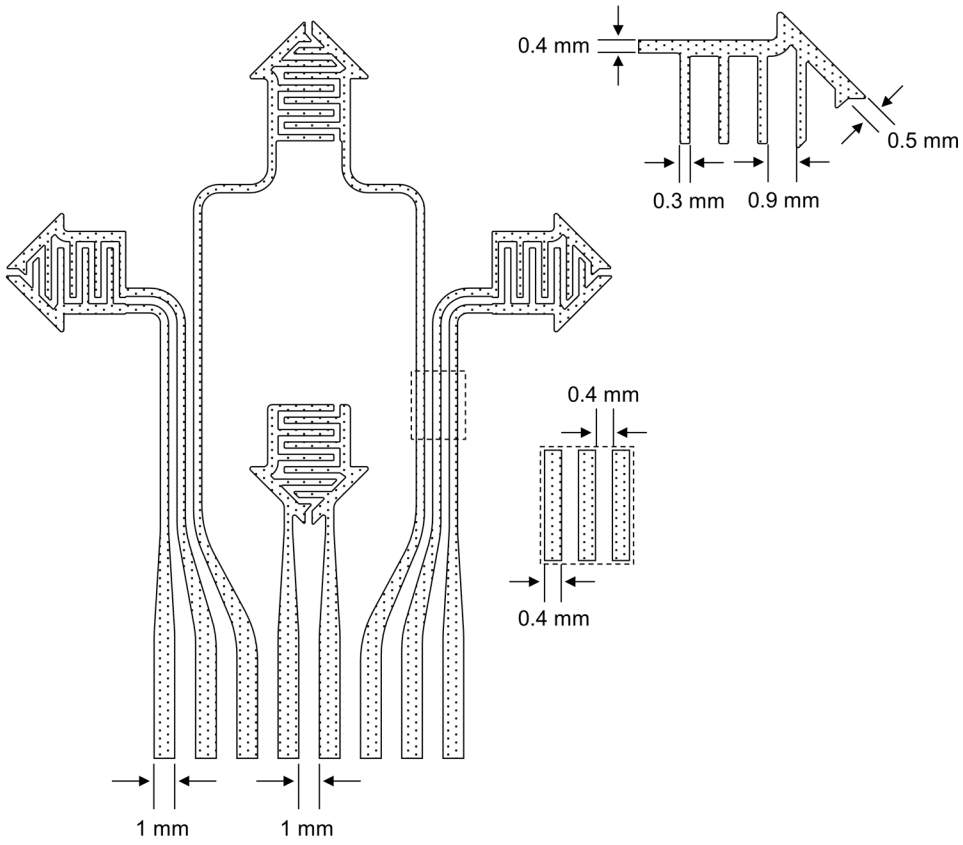


**Supplementary Fig. 50 Mechanical pattern design of the bottom electrode of the tactile sensor.**

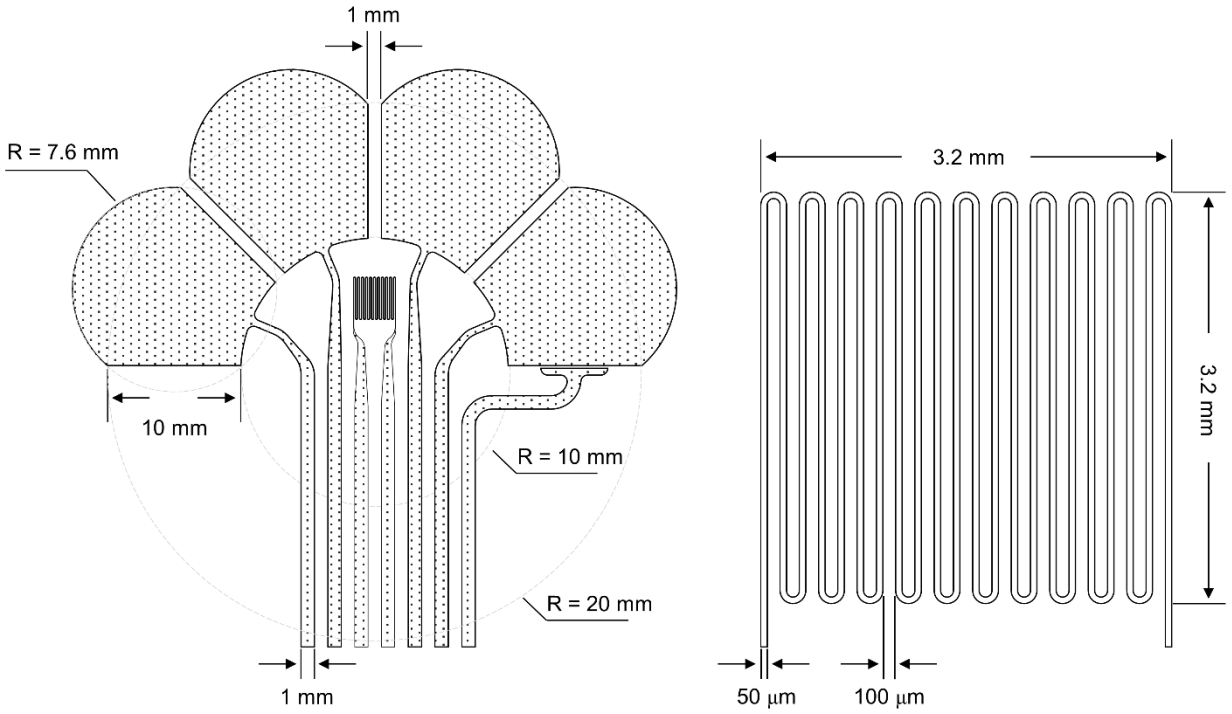


**Supplementary Fig. 51 Mechanical pattern design of the bottom electrode of the visual temperature sensor.** The inset shows the magnified view of the Au serpentine trace.

## Supplementary Tables

**Supplementary Table 1 Turn-on delay values for PeACEL device.**

| $f_{sw}$ (Hz) | $f_{ac}$ ($V_{ac}$=100V) | Turn-on delay (ms) |
|---|---|---|
| 20 | 1 kHz | 0.14 |
| | 10 kHz | 0.17 |
| | 20 kHz | 0.18 |
| 50 | 1 kHz | 0.22 |
| | 10 kHz | 0.26 |
| | 20 kHz | 0.25 |

**Supplementary Table 2 Summary of the composition and performances of stretchable powder-based ACEL devices.**

| Phosphors | Polymer matrix | Colour | Electrode | Stretchability | Reference |
|---|---|---|---|---|---|
| PeZS | SEBS | Blue–Red (Full colour) | AgNWs | 400% | This work |
| | | | Hydrogels | 1000% | |
| ZnS: Cu | PDMS | Blue | AgNWs | 100% | 27 |
| ZnS: Cu | TPU | Blue | AgNWs | 100% | 28 |
| ZnS: Cu | PDMS | Blue | AgNWs | 90% | 29 |
| ZnS: Cu | PUU | Blue | AgNWs | 150% | 30 |
| ZnS: Ag,<br>ZnS: Cu,<br>ZnS: Cu, Mn | PEDUB | Blue<br>Green<br>Orange | AgNWs | 110% | 31 |
| ZnS: Cu | PDMS | Blue | AgNWs | 150% | 32 |
| ZnS: Cu | PVDF-HFP | Blue | AgNWs | 100% | 33 |
| ZnS: Cu | Ecoflex | Green | AgNW/CNT | 85% | 34 |
| ZnS: Mn | PDMS | Blue | AgNW/PEDOT: PSS | 85% | 35 |
| ZnS: Cu<br>$MAPbBr_3$ | PDMS | Green | Ionic hydrogel | 180% | 22 |
| ZnS: Cu<br>ZnS: Mn | (PVDF)-based fluoroelastomer | Blue<br>Orange | Self-healing ionogels | 800% | 36 |
| ZnS: Cu, Cl | Ecoflex | Blue | Ionogels | 1200% | 37 |
| ZnS: Cu | Ecoflex | Blue | Ionogel | 700% | 38 |
| ZnS powders | Acrylic elastomer (VHB 4910, 3M) | Blue | Hydrogels | 1500% | 39 |
| ZnS: Cu | PDMS)/liquid electrolyte | Blue | Ionogel | 350% | 40 |

## Supplementary Videos

**Supplementary Video 1 Flexible PeACEL array on skin.**

**Supplementary Video 2 Demonstration of the visual temperature sensing.**

**Supplementary Video 3 Sensory visualization in soft robotic system.**

## References


1. Sun, M.-J. et al. In situ visualization of assembly and photonic signal processing in a triplet light-harvesting nanosystem. *J. Am. Chem. Soc.* **140**, 4269-4278 (2018).
2. Xie, Z. et al. Wide-range lifetime-tunable and responsive ultralong organic phosphorescent multi-host/guest system. *Nat. Commun.* **12**, 3522 (2021).
3. Hintermayr, V. A. et al. Polymer nanoreactors shield perovskite nanocrystals from degradation. *Nano Lett.* **19**, 4928-4933 (2019).
4. Edhborg, F., Küçüköz, B. l., Gray, V. & Albinsson, B. Singlet energy transfer in anthracene–porphyrin complexes: mechanism, geometry, and implications for intramolecular photon upconversion. *J. Phys. Chem. B* **123**, 9934-9943 (2019).
5. Bredol, M. & Schulze Dieckhoff, H. Materials for powder-based AC-electroluminescence. *Materials* **3**, 1353-1374 (2010).
6. Villalobos, G. R. et al. Protective silica coatings on zinc-sulfide-based phosphor particles. *J. Am. Ceram. Soc.* **85**, 2128-2130 (2002).
7. Guo, C., Chu, B., Wu, M. & Su, Q. Oxide coating for alkaline earth sulfide based phosphor. *J. Lumin.* **105**, 121-126 (2003).
8. Park, W. et al. Uniform and continuous $Y_2O_3$ coating on ZnS phosphors. *Mater. Sci. Eng., B* **76**, 122-126 (2000).
9. Guo, C., Chu, B. & Su, Q. Improving the stability of alkaline earth sulfide-based phosphors. Appl. Surf. Sci. 225, 198-203 (2004).
10. Reckow, J. et al. Tolerability and blinding of 4x1 high-definition transcranial direct current stimulation (HD-tDCS) at two and three milliamps. *Brain Stimul.* **11**, 991-997 (2018).
11. Kim, M. H., Hong, S. M. & Koo, C. M. Electric actuation properties of SEBS/CB and SEBS/SWCNT nanocomposite films with different conductive fillers. *Macromol. Res.* **20**, 59-65 (2012).
12. Gerratt, A. P. & Bergbreiter, S. Dielectric breakdown of PDMS thin films. *J. Micromech. Microeng.* **23**, 067001 (2013).
13. Larson, C. et al. Highly stretchable electroluminescent skin for optical signaling and tactile sensing. *Science* **351**, 1071-1074 (2016).
14. Zhao, C. et al. Fully screen-printed, multicolor, and stretchable electroluminescent displays for

epidermal electronics. *ACS App. Mater. Interfaces* **12**, 47902-47910 (2020).

15. Zhang, Z. et al. Textile display for electronic and brain-interfaced communications. *Adv. Mater.* **30**, 1800323 (2018).
16. Jeong, S. M. et al. Bright, wind-driven white mechanoluminescence from zinc sulphide microparticles embedded in a polydimethylsiloxane elastomer. *Energy Environ. Sci.* **7**, 3338-3346 (2014).
17. Shi, X. et al. Large-area display textiles integrated with functional systems. *Nature* **591**, 240-245 (2021).
18. Zuo, Y. et al. Flexible color-tunable electroluminescent devices by designing dielectric-distinguishing double-stacked emissive layers. *Adv. Funct. Mater.* **30**, 2005200 (2020).
19. Li, S., Peele, B. N., Larson, C. M., Zhao, H. & Shepherd, R. F. A stretchable multicolor display and touch interface using photopatterning and transfer printing. *Adv. Mater.* **28**, 9770-9775 (2016).
20. Zhang, P. et al. Integrated 3D printing of flexible electroluminescent devices and soft robots. *Nat. Commun.* **13**, 4775 (2022).
21. Zhang, X. et al. Sustainable and transparent fish gelatin films for flexible electroluminescent devices. *ACS Nano* **14**, 3876-3884 (2020).
22. Zhou, H. et al. Water passivation of perovskite nanocrystals enables air-stable intrinsically stretchable color-conversion layers for stretchable displays. *Adv. Mater.* **32**, 2001989 (2020).
23. Park, J.-M. et al. Aromatic nonpolar organogels for efficient and stable perovskite green emitters. *Nat. Commun.* **11**, 4638 (2020).
24. Wang, Y. et al. Solid-state displacement synthesis of alkaline-earth selenide for white emission through alternating current electroluminescence. *ACS Materials Lett.* **4**, 2447-2453 (2022).
25. Li, Y., Song, R., Liu, J., Qian, J. & Wang, X. Printable and writable $CsPbBr_3/Cs_4PbBr_6$ perovskite quantum dots as fluorescent inks for down-conversion flexible ACEL devices. *ACS Appl. Nano Mater.* **5**, 18288-18296 (2022).
26. Zhao, C. et al. Bright stretchable white alternating-current electroluminescent devices enabled by photoluminescent phosphor. *Adv. Mater. Technol.* **7**, 2101440 (2022).
27. Wang, J., Yan, C., Chee, K. J. & Lee, P. S. Highly stretchable and self-deformable alternating current electroluminescent devices. *Adv. Mater.* **27**, 2876-2882 (2015).

28. Zhou, Y. et al. Bright stretchable electroluminescent devices based on silver nanowire electrodes and high-k thermoplastic elastomers. *ACS App. Mater. Interfaces* **10**, 44760-44767 (2018).
29. Stauffer, F. & Tybrandt, K. Bright stretchable alternating current electroluminescent displays based on high permittivity composites. *Adv. Mater.* **28**, 7200-7203 (2016).
30. You, B., Kim, Y., Ju, B.-K. & Kim, J.-W. Highly stretchable and waterproof electroluminescence device based on superstable stretchable transparent electrode. *ACS App. Mater. Interfaces* **9**, 5486-5494 (2017).
31. Shin, Y. B. et al. Self-integratable, healable, and stretchable electroluminescent device fabricated via dynamic urea bonds equipped in polyurethane. *ACS App. Mater. Interfaces* **12**, 10949-10958 (2020).
32. Cho, S. et al. Highly stretchable sound-in-display flectronics based on strain-insensitive metallic nanonetworks. *Adv. Sci.* **8**, 2001647 (2021).
33. Zhou, Y. et al. Stretchable high-permittivity nanocomposites for epidermal alternating-current electroluminescent displays. *ACS Materials Lett.* **1**, 511-518 (2019).
34. Lee, Y. R. et al. Electroluminescent soft elastomer actuators with adjustable luminance and strain. *Soft Matter* **15**, 7996-8000 (2019).
35. Shin, H. et al. Stretchable electroluminescent display enabled by graphene-based hybrid electrode. *ACS App. Mater. Interfaces* **11**, 14222-14228 (2019).
36. Tan, Y. J. et al. A transparent, self-healing and high-κ dielectric for low-field-emission stretchable optoelectronics. *Nat. Mater.* **19**, 182-188 (2020).
37. Dinh Xuan, H. et al. Super stretchable and durable electroluminescent devices based on double-network ionogels. *Adv. Mater.* **33**, 2008849 (2021).
38. Wang, J. et al. Extremely stretchable electroluminescent devices with ionic conductors. *Adv. Mater.* **28**, 4490-4496 (2016).
39. Yang, C. H., Chen, B., Zhou, J., Chen, Y. M. & Suo, Z. Electroluminescence of giant stretchability. *Adv. Mater.* **28**, 4480-4484 (2016).
40. Shi, L. et al. Improving dielectric constant of polymers through liquid electrolyte inclusion. *Adv. Funct. Mater.* **31**, 2007863 (2021).